

# Scalable Evaluation Framework for Foundation Models in Musculoskeletal MRI Bridging Computational Innovation with Clinical Utility

Gabrielle Hoyer<sup>1,2,3\*</sup>, Michelle W Tong<sup>1,2,3</sup>, Rupsa Bhattacharjee<sup>1</sup>, Valentina Pedoia<sup>1</sup>, Sharmila Majumdar<sup>1,2,3</sup>

<sup>1</sup>*Department of Radiology and Biomedical Imaging, University of California, San Francisco, San Francisco, CA, USA*

<sup>2</sup>*Department of Bioengineering, University of California Berkeley, Berkeley, CA, USA*

<sup>3</sup>*Department of Bioengineering, University of California San Francisco, San Francisco, CA, USA*

\* Correspondence: [gabbie.hoyer@ucsf.edu](mailto:gabbie.hoyer@ucsf.edu)

## Abstract

Foundation models hold transformative potential for medical imaging, but their clinical utility requires rigorous evaluation to address their strengths and limitations. This study introduces an evaluation framework for assessing the clinical impact and translatability of SAM, MedSAM, and SAM2, using musculoskeletal MRI as a case study. We tested these models across zero-shot and finetuned paradigms to assess their ability to process diverse anatomical structures and effectuate clinically reliable biomarkers, including cartilage thickness, muscle volume, and disc height. We engineered a modular pipeline emphasizing scalability, clinical relevance, and workflow integration, reducing manual effort and aligning validation with end-user expectations. Hierarchical modeling revealed how dataset mixing, anatomical complexity, and MRI acquisition parameters influence performance, providing insights into the role of imaging refinements in improving segmentation accuracy. This work demonstrates how clinically focused evaluations can connect computational advancements with tangible applications, creating a pathway for foundation models to address medical challenges. By emphasizing interdisciplinary collaboration and aligning technical innovation with clinical priorities, our framework provides a roadmap for advancing machine learning technologies into scalable and impactful biomedical solutions.

## Introduction

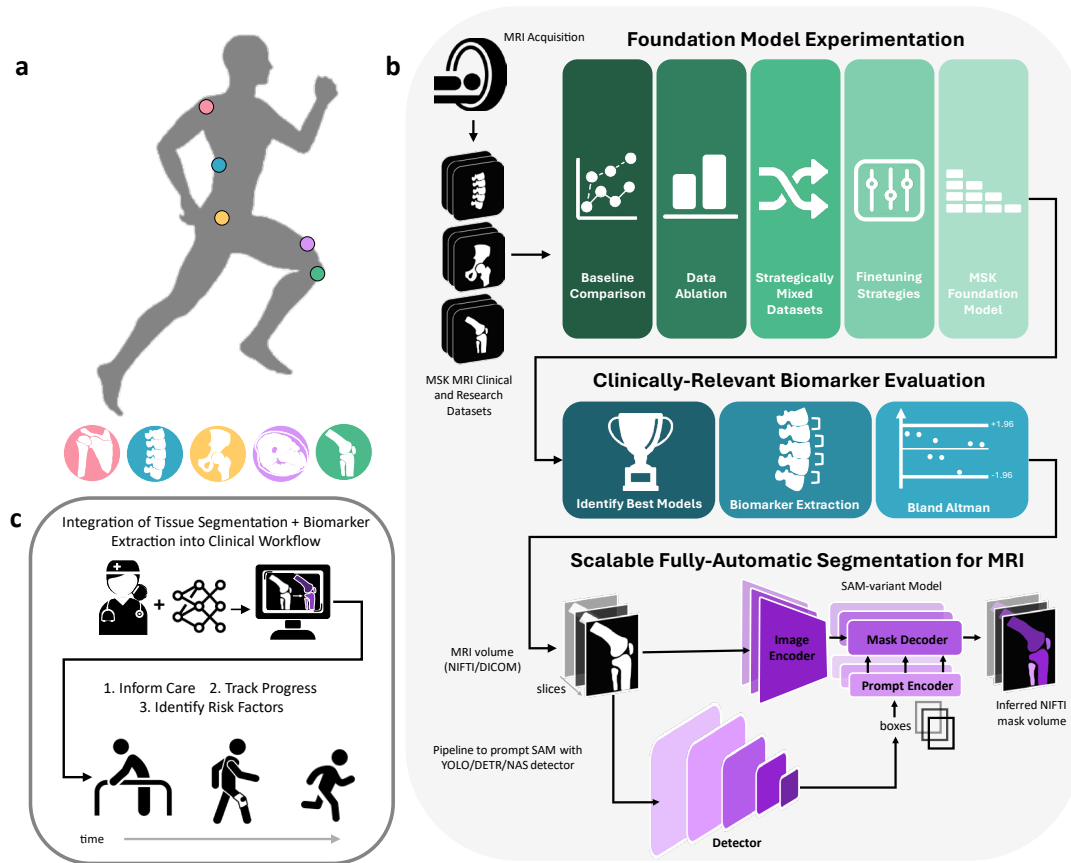
In medical image processing, reliable segmentation models are foundational for advancing image analysis, driving imaging biomarker discovery, and developing diagnostic and prognostic tools<sup>1,2</sup>. Early architectures, such as U-Net<sup>3</sup>, introduced an encoder-decoder design capable of producing accurate segmentations from limited training data. Subsequent work expanded on this innovation to volumetric imaging with V-Net<sup>4</sup> and refined feature representations through Unet++<sup>5</sup> and ResUnet++<sup>6</sup>. Further, the Attention U-Net<sup>7</sup> addressed smaller or harder-to-segment regions by incorporating attention mechanisms, and nnU-Net<sup>8</sup> accelerated generalization via automated model adaptation. More recently, transformer-based Swin-Unet<sup>9</sup> introduced global context awareness into biomedical segmentation tasks.

Despite advances, generalizing to new anatomies or imaging protocols remains difficult<sup>10</sup>, as models trained on specific datasets or imaging modalities often underperform when exposed to different MRI sequences, vendors, or anatomical regions<sup>11,12</sup>. Emerging foundation models, such as the Segment Anything Model (SAM)<sup>13</sup> and SAM2<sup>14</sup>, have shown promise in natural image segmentation, prompting investigations into their potential across medical modalities like CT, ultrasound, and MRI<sup>15–22</sup>. However, these broad applications often overlook the distinct challenges posed by imaging physics<sup>23</sup>, acquisition protocols, and clinical imperatives<sup>24,25</sup>, potentially limiting their real-world utility despite domain-specific adaptations.

Musculoskeletal (MSK) MRI exemplifies the domain-specific challenges that foundation models must address, and provides a focused yet diverse case study for evaluating model performance and system design in translational biomedical innovation. This imaging modality captures multiple tissue types (e.g., bone, cartilage, soft tissue) within a single exam; additionally, it presents complex segmentation requirements

that mirror the varied technical demands of clinical practice. With broad imaging and anatomical variability, MSK MRI serves as an ideal platform for rigorously testing segmentation models under conditions that combine clinical relevance with technological complexity. Surpassing the simplicity of single-label tasks, tissue<sup>26–28</sup> segmentation in MSK challenges models to evaluate anatomical interdependence; it also necessitates distinguishing tissues with differing properties across MRI sequences, which is vital for understanding MSK conditions. Musculoskeletal disorders contribute significantly to global disability<sup>29–31</sup> but have historically received less focus in research and innovation compared to fields like oncology and neurology<sup>32</sup>, which often draw broader public and academic attention. Yet, the inherent technical complexity and clinical relevance of MSK imaging provide unique opportunities to advance segmentation methodologies. These datasets may, therefore, demonstrate how foundation models can address clinically meaningful yet underserved areas of healthcare.

**Figure 1: Overview of the study design and objectives for musculoskeletal MRI segmentation.**



**a)** Visual representation of the anatomical regions included in the study, covering the shoulder (pink), spine (blue), hip (yellow), thigh (purple), and knee (green).

**b)** Workflow of foundation model experimentation, integrating musculoskeletal MRI datasets for large-scale evaluation and optimization of segmentation models (SAM, SAM2, MedSAM). The study investigates zero-shot baseline performance, dataset ablation, strategic mixing, finetuning strategies, and the potential for constructing a specialized musculoskeletal (MSK) foundation model. Clinically relevant biomarkers are extracted from the best-performing models, with statistical comparison to manual annotations (e.g., Bland-Altman plots), followed by scalable, fully automatic segmentation pipelines for MRI using detection model prompt generation.

**c)** Conceptual framework for integrating automatic tissue segmentation and biomarker extraction into clinical workflows to inform care, track progress, and identify patient risk factors.

Given these complexities, traditional segmentation metrics alone are insufficient, necessitating an emphasis on clinically meaningful measures. While traditional metrics like Dice and IoU are frequently used, they can lead to biased results<sup>33,34</sup> if applied without consideration of clinically meaningful measures. Our study, therefore, extends its assessment of these models by undergoing the extraction of clinically relevant biomarkers via segmentation; these features provide insight into disease progression and aid treatment planning for conditions including knee osteoarthritis<sup>35</sup>, lumbar spinal stenosis<sup>36</sup>, and thigh sarcopenia<sup>37</sup>. In addition to traditional segmentation metrics, we extract values for cartilage thickness<sup>38-40</sup>, T<sub>1</sub>ρ /T<sub>2</sub> mapping<sup>41-43</sup>, disc height<sup>44,45</sup>, and tissue volume<sup>46-52</sup>, which more directly reflect anatomical and pathological nuances.

Addressing the challenges of MSK MRI segmentation requires developing modular, fully automated pipelines<sup>53,54</sup> that support diverse models and architectures without manual prompts, especially for 3D datasets with hundreds of slices per scan. Such modularity enables continuous refinement by integrating emerging components, including detection mechanisms, segmentation models, and biomarker computation tools. Evaluations should systematically identify limitations while assessing how each component contributes to performance (e.g., data efficiency, speed, resource use)<sup>55</sup> and whether newer alternatives provide meaningful improvements. This balanced framework ensures pipelines remain adaptable to advancements while meeting the technical demands of clinical scalability.

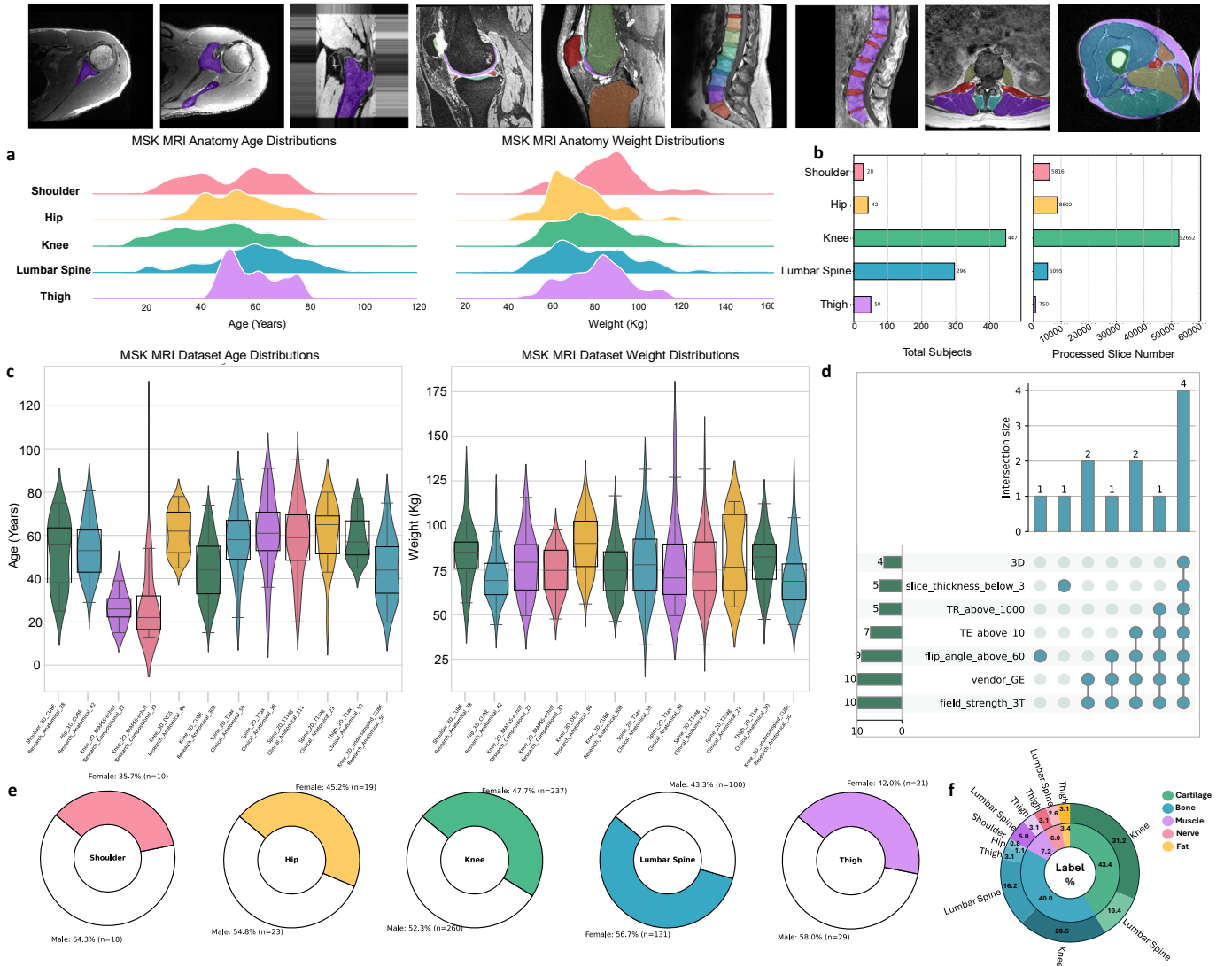
Our study (Figure 1) tackles multifaceted challenges associated with foundation model segmentation in the context of MSK MRI by rigorously evaluating SAM, MedSAM, and SAM2 using zero-shot and finetuned approaches. We emphasize clinically relevant benchmarks, such as biomarker accuracy, to assess a model's practical value in diagnosing and managing MSK conditions. By leveraging modular pipeline designs and biomarker extraction, we aim to establish a framework for systematically evaluating segmentation models and translating them into tools that serve the needs of radiologists and clinical teams. This structured approach bridges the gap between segmentation advancements and clinical translation, while establishing a roadmap for creating adaptable, scalable solutions to address evolving healthcare needs<sup>56</sup>. We aim to advance the integration of foundation models into workflows that are impactful and adaptable to real-world medical imaging challenges by promoting interdisciplinary collaboration and clinical relevance.

## **Results**

### *MSK Dataset Overview*

We utilized various musculoskeletal MRI datasets covering key anatomical regions (i.e. knee, hip, lumbar spine, shoulder, and thigh), as well as diverse clinical and research imaging protocols (Figure 2). Dataset naming conventions, anatomical labels, and demographic characteristics are provided in Supplementary Tables S0–S2. This assortment of annotated medical imaging data constitutes a solid basis for evaluating multi-tissue segmentation models across diverse anatomical and clinical contexts, leveraging their diversity to address both common and anatomically complex segmentation tasks.

**Figure 2: Overview of dataset characteristics, demographic distributions, and MRI acquisition parameters.**



**a)** Age and weight distribution for each musculoskeletal anatomy group (shoulder, hip, knee, lumbar spine, thigh) represented as density plots.

**b)** Total number of subjects and processed slices (slices with available segmentation masks) for each anatomy group.

**c)** Violin plots showing age and weight distributions for individual datasets, categorized by anatomical region, MRI sequence type, and protocol specifications (research vs. clinical, anatomical vs. compositional focus).

**d)** Upset plot displays the intersection of MRI acquisition parameters, including field strength, slice thickness, TR, TE, flip angle, 3D imaging, and vendor details.

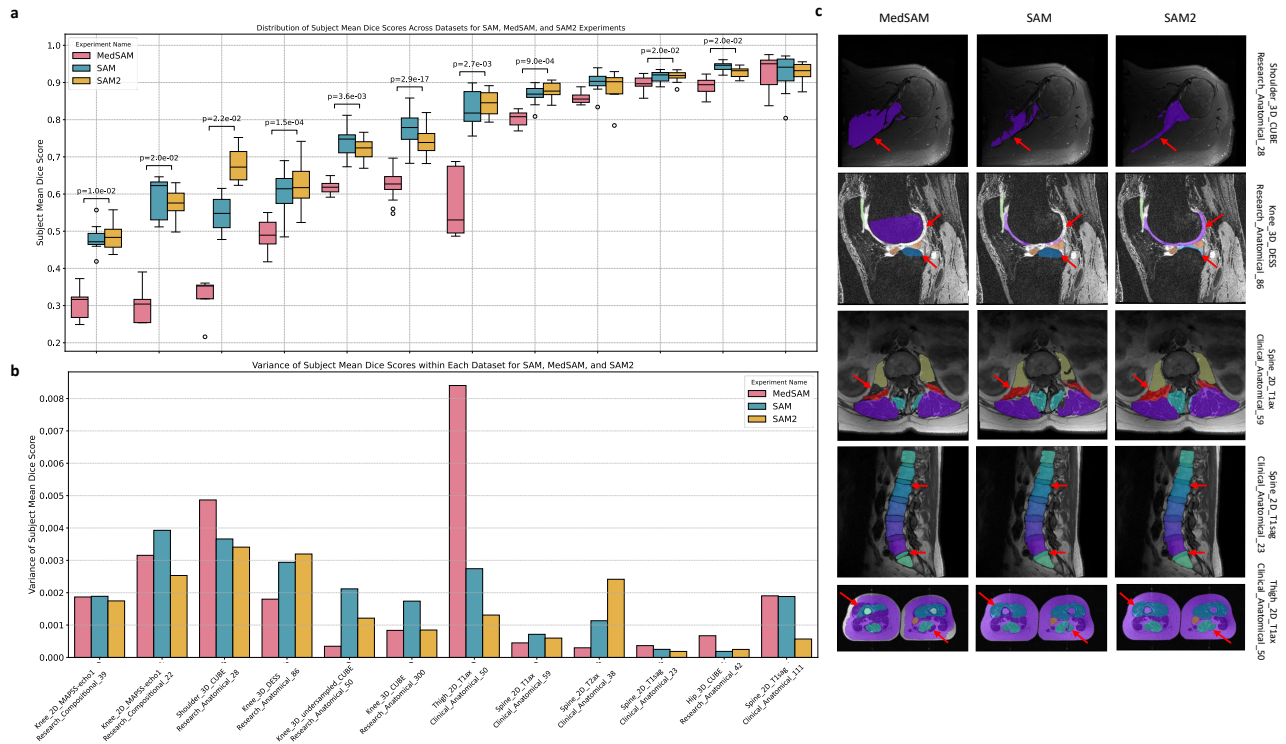
**e)** Donut plots displaying the sex distribution (male vs. female) within each anatomy group, with percentages and total subject counts.

**f)** Layered donut plot illustrating the distribution of tissue segmentation labels (cartilage, bone, muscle, nerve, fat) across the entire dataset. The inner layer shows the percentage of each tissue type, while the outer layer details how tissue types are distributed across anatomical regions.

## Baseline Model Performance in Zero-shot Segmentation

Figure 3a shows the mean Dice scores for MedSAM, SAM, and SAM2 across datasets (Supplementary Table S3). The Friedman test with Benjamini-Hochberg correction revealed that SAM and SAM2 frequently outperformed MedSAM. In the Shoulder\_3D\_CUBE\_Research\_Anatomical\_28 dataset, SAM2 achieved a Dice score of 0.680, significantly higher than SAM's 0.547 and MedSAM's 0.320 ( $P = 0.022$ ). Similarly, in Thigh\_2D\_T1ax\_Clinical\_Anatomical\_50, SAM2 reached 0.843, SAM followed at 0.831, and MedSAM lagged at 0.580 ( $P = 2.74E-03$ ). Moreover, in datasets such as Thigh\_2D\_T1ax\_Clinical\_Anatomical\_50, MedSAM exhibited higher subject-level performance variance, while SAM2 achieved more consistent results.

**Figure 3: Baseline performance comparison of MedSAM, SAM, and SAM2 models on musculoskeletal MRI datasets.**



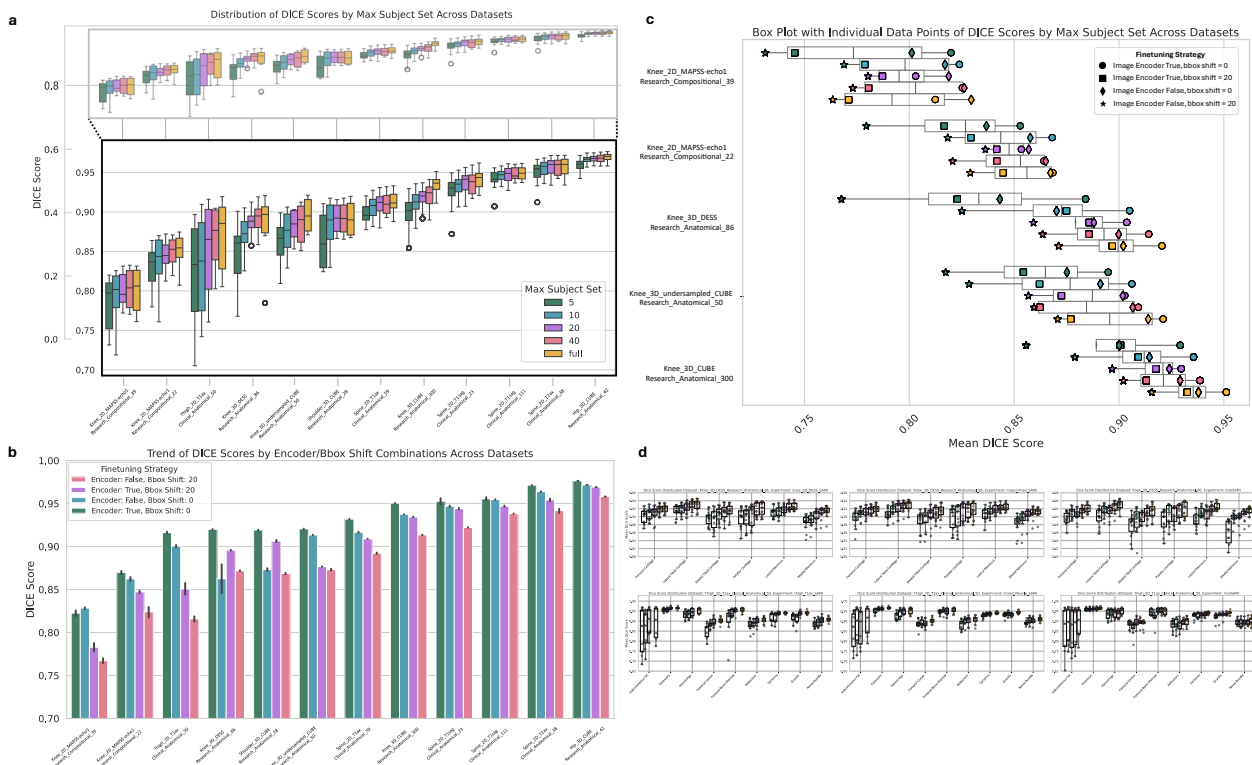
**a)** Box plots comparing the distribution of subject mean Dice scores across different datasets for MedSAM (pink), SAM (blue), and SAM2 (yellow). Friedman Test p-values, corrected using Benjamini-Hochberg FDR adjustment, are shown above the box plots, indicating significant differences between the models. Further details, including Benjamini-Hochberg FDR-corrected p-values, are listed Supplementary Table 4.

**b)** Bar plots showing the variance of subject mean Dice scores within each dataset for the three models (MedSAM, SAM, SAM2).

**c)** Representative segmentation overlays from MedSAM, SAM, and SAM2 (left to right) for five MRI datasets: Shoulder\_3D\_CUBE\_Research\_Anatomical\_28 (scapula), Knee\_3D\_DESS\_Research\_Anatomical\_86 (femoral, patellar, and tibial cartilage, menisci), Spine\_2D\_T1ax\_Clinical\_Anatomical\_59 (Erector spinae, multifidus, psoas, quadratus lumborum), Spine\_2D\_T1sag\_Clinical\_Anatomical\_23 (vertebral bodies and intervertebral discs), and Thigh\_2D\_T1ax\_Clinical\_Anatomical\_50 (muscle groups, femoral bone, subcutaneous fat, neurovascular structures). The segmentations with red arrows offer a qualitative comparison of segmentation accuracy and tissue boundary definition across different anatomical regions (e.g. bone, cartilage, muscle, and fat) between models.

In Knee\_3D\_DESS\_Research\_Anatomical\_86, SAM2 (0.624) and SAM (0.610) surpassed MedSAM (0.488,  $P = 1.54E-04$ ), with pairwise Wilcoxon tests reinforcing the superior performance of SAM and SAM2 to MedSAM in this task ( $P = 8.79E-04$ ). These results, representative of broader trends across datasets (Supplementary Tables S4 and S5), highlight SAM2's improved performance in anatomically complex tasks, such as the thigh and shoulder, while MedSAM exhibited comparatively lower performance in most tasks (Figure 3b). Notwithstanding, datasets like Spine\_2D\_T1sag\_Clinical\_Anatomical\_111, with uniformly defined segmentation tasks, showed no significant performance differences among models ( $P = 0.127$ ), likely due to lower task complexity. Figure 3c provides visual overlays accentuating differences in segmentation accuracy and tissue boundary delineation.

**Figure 4: Evaluation of Finetuning Strategies for SAM Models in Musculoskeletal MRI**



**a) Dice Score Distributions by Subject Set Size:** Box plots showing Dice score distributions for the mskSAM experiment across subject set sizes (5, 10, 20, 40, full dataset). Each set size is color-coded (green, blue, purple, pink, yellow), and the y-axis represents mean Dice scores. The inset zooms in on the higher score range for clarity.

**b) Comparison of Finetuning Strategies with Full Subject Sets:** Bar plots showing mean Dice scores for musculoskeletal MRI datasets under four finetuning strategies, applied to full subject sets. Strategies are color-coded: Encoder False, Bbox Shift 20 (pink); Encoder True, Bbox Shift 20 (purple); Encoder False, Bbox Shift 0 (blue); Encoder True, Bbox Shift 0 (green). Error bars show variability across test subjects.

**c) Dice Score Distributions for Knee-Related Datasets:** Box plots for knee-related datasets from mskSAM finetuning, comparing subject set sizes (5, 10, 20, 40, full) and finetuning strategies. Black-and-white box plots show overall Dice distributions, while colored symbols represent specific finetuning strategies (circle, square, diamond, star) corresponding to strategies in panel b.

**d) Dice Score Distributions for Knee and Thigh Datasets:** Box plots for the Knee\_3D\_DESS and Thigh\_2D\_T1ax datasets, comparing single-dataset finetuning, mixed-dataset finetuning, and mskSAM finetuning across subject set sizes. Top Row: Knee\_3D\_DESS results under three finetuning conditions (single-knee, all-knee, all musculoskeletal). Bottom Row: Thigh\_2D\_T1ax results for finetuning on the thigh alone, thigh + spine muscle, and all musculoskeletal datasets. Colored symbols match finetuning strategies from panel c.

### *Strategies for Finetuning and Tactical Data Usage*

We further investigated finetuning strategies to optimize segmentation models for MSK MRI tasks; specifically, we examined the effect of finetuning parameters, training set sizes, and tactical dataset mixing on downstream segmentation performance. Our exploration extended to finetuning each SAM, SAM2, and MedSAM baseline model using our extensive MSK MRI dataset to construct a potential MSK MRI-specific foundation model. Supplementary Table S6 contains experimental details on variations in anatomical regions, label complexities, and MRI sequences found in the finetuning sets.

### *Impact of Dataset Size on Model Adaptation*

We systematically analyzed the impact of training dataset size (5, 10, 20, 40, full) on finetuned SAM models (Figure 4a). Larger training sets generally yielded higher Dice scores, demonstrating the importance of comprehensive datasets for improved model generalization. Consistent performance was observed in datasets like `Knee_3D_CUBE_Research_Anatomical` and `Spine_2D_T1sag_Clinical_Anatomical_111`, even with smaller training sets. This was likely due to uniform segmentation tasks across subjects, with anatomical simplicity particularly stabilizing results in the spine dataset. In contrast, the `Knee_2D_MAPSS-echo1` sequence, optimized for cartilage imaging but limited by lower spatial resolution and large slice thickness, exhibited performance variability across training sizes. Similarly, challenges with anatomical label complexity and cohort diversity persisted in datasets such as `Shoulder_3D_CUBE` and `Thigh_2D_T1ax`; this signals the need for bespoke finetuning strategies for more convoluted clinical and quantitative imaging use cases, even as training set sizes increase.

### *Impact of Image Encoder and Bounding Box Shift*

We assessed four strategies combining image encoder finetuning and bounding box shift augmentation: finetuning both components or freezing the encoder, each with or without a shift of 20. Figure 4b shows that finetuning both components without bounding box shift consistently yielded the highest Dice scores, especially in datasets with complex anatomical tasks (e.g., `Thigh_2D_T1ax_Clinical_Anatomical_50`, `Shoulder_3D_CUBE_Research_Anatomical_28`). In contrast, simpler datasets (e.g., `Spine_2D_T1sag_Clinical_Anatomical_111`, `Hip_3D_CUBE_Research_Anatomical_42`) showed minimal differences across strategies, suggesting reduced sensitivity to encoder adjustments. Bounding box shift augmentation had limited overall impact, with no significant benefit observed in uniform anatomical tasks.

### *Impact of Dataset Size and Finetuning Strategies in Knee MRI*

To validate trends observed across anatomies, we examined knee MRI datasets as a focused case study (Figure 4c, Supplementary Figure 1). Finetuning both the image encoder and mask decoder without bounding box perturbation achieved the highest Dice scores, particularly in smaller training sets with cohort variability. As subject set sizes increased, performance differences across strategies diminished, aligning with findings from other anatomies. High-resolution datasets (e.g., `Knee_3D_CUBE_Research_Anatomical`) maintained stable performance across strategies, while lower-resolution datasets (e.g., `Knee_2D_MAPSS-echo1_Research_Compositional_39`) exhibited greater variability, especially with smaller training sets, confirming the compounded effects of anatomical complexity and resolution constraints on finetuning efficacy.

**Table 1: Tiered Analysis of Baseline and Finetuned SAM Models for MSK MRI Datasets to Uncover Label- and Tissue-Level Performance Dynamics**

| MSK Dataset   | SAM               |                          | SAM2                    |                    | MedSAM              |                    |             |          |              |             |
|---|-------------------|--------------------------|-------------------------|--------------------|---------------------|--------------------|-------------|----------|--------------|-------------|
|   | Base              | Fine-tuned               | Base                    | Fine-tuned         | Base                | Fine-tuned         |             |          |              |             |
| <b>Hip, Thigh, and Shoulder Datasets</b>                |                   |                          |                         |                    |                     |                    |             |          |              |             |
| Hip_3D_CUBE_42  | 0.94269           | <b>0.97634</b>           | 0.92695                 | 0.97648            | 0.88986             | 0.97517            |             |          |              |             |
| Thigh_2D_T1ax_50  | 0.83106           | 0.91212                  | 0.84252                 | 0.90117            | 0.58037             | <b>0.91513</b>     |             |          |              |             |
| Shoulder_3D_CUBE_28                                     | 0.54722           | 0.91972                  | 0.68011                 | <b>0.92343</b>     | 0.32046             | 0.91887            |             |          |              |             |
| <b>Spine Datasets</b>                                   |                   |                          |                         |                    |                     |                    |             |          |              |             |
| Spine_2D_T1ax_59  | 0.61008           | 0.92051                  | 0.62420                 | <b>0.93469</b>     | 0.48823             | 0.92006            |             |          |              |             |
| Spine_2D_T2ax_38  | 0.89893           | <b>0.97087</b>           | 0.88297                 | 0.97000            | 0.85851             | 0.96889            |             |          |              |             |
| Spine_2D_T1sag_23                                       | 0.91586           | <b>0.96097</b>           | 0.91670                 | 0.95993            | 0.89896             | 0.95886            |             |          |              |             |
| Spine_2D_T1sag_111                                      | 0.92899           | 0.96049                  | 0.92807                 | 0.95989            | 0.92629             | <b>0.96104</b>     |             |          |              |             |
| <b>Knee Datasets</b>                                    |                   |                          |                         |                    |                     |                    |             |          |              |             |
| Knee_MAPPS_22   | 0.58875           | 0.86849                  | 0.57235                 | <b>0.87667</b>     | 0.30382             | 0.86944            |             |          |              |             |
| Knee_MAPPS_39   | 0.48063           | 0.81239                  | 0.48615                 | <b>0.82911</b>     | 0.30285             | 0.82140            |             |          |              |             |
| Knee_3D_DESS_86   | 0.61008           | 0.92051                  | 0.62420                 | <b>0.93469</b>     | 0.48823             | 0.92006            |             |          |              |             |
| Knee_3D_CUBE_300  | 0.77414           | 0.95125                  | 0.73852                 | <b>0.95127</b>     | 0.62701             | 0.94917            |             |          |              |             |
| Knee_3D_CUBE_Undersampled_50                            | 0.73839           | <b>0.92105</b>           | 0.71945                 | 0.92026            | 0.61821             | 0.92006            |             |          |              |             |
| <b>Dataset</b>  | <b>Experiment</b> | <b>Muscle</b>            | <b>Bone</b>             | <b>Nerve</b>       | <b>Fat</b>          | <b>Mean Tissue</b> |             |          |              |             |
| Thigh_2D<br>T1ax_50                                     | SAM               | 0.90313                  | 0.85958                 | 0.84700            | 0.71454             | 0.83106            |             |          |              |             |
|   | SAM2              | 0.87589                  | 0.88268                 | 0.84811            | 0.76339             | 0.84252            |             |          |              |             |
|   | MedSAM            | 0.76438                  | 0.60922                 | 0.59509            | 0.35280             | 0.58037            |             |          |              |             |
|   | <b>mSkSAM2</b>    | <b>0.93650</b>           | <b>0.92218</b>          | <b>0.89448</b>     | <b>0.85150</b>      | <b>0.90117</b>     |             |          |              |             |
|   |                   | <b>Cartilage</b>         | <b>Bone</b>             | <b>Nerve</b>       | <b>Fat</b>          | <b>Mean Tissue</b> |             |          |              |             |
| Spine_2D<br>T2ax_38                                     | SAM               | 0.95644                  | 0.87317                 | 0.86719            | 0.89893             | 0.88297            |             |          |              |             |
|   | SAM2              | 0.95759                  | 0.89917                 | 0.79216            | 0.88297             | 0.88297            |             |          |              |             |
|   | MedSAM            | 0.90607                  | 0.88370                 | 0.78575            | 0.85851             | 0.85851            |             |          |              |             |
|   | <b>mSkSAM2</b>    | <b>0.97697</b>           | <b>0.96453</b>          | <b>0.96850</b>     | <b>0.97000</b>      | <b>0.97000</b>     |             |          |              |             |
|   |                   | <b>Cartilage</b>         | <b>Bone</b>             | <b>Nerve</b>       | <b>Fat</b>          | <b>Mean Tissue</b> |             |          |              |             |
| Spine_2D<br>T1sag_23                                    | SAM               | 0.89954                  | 0.93217                 | 0.91586            | 0.89893             | 0.89893            |             |          |              |             |
|   | SAM2              | 0.90159                  | 0.93180                 | 0.91670            | 0.89893             | 0.89893            |             |          |              |             |
|   | MedSAM            | 0.86398                  | 0.93393                 | 0.89896            | 0.89893             | 0.89893            |             |          |              |             |
|   | <b>mSkSAM2</b>    | <b>0.95584</b>           | <b>0.96402</b>          | <b>0.95993</b>     | <b>0.95993</b>      | <b>0.95993</b>     |             |          |              |             |
| Spine_2D<br>T1sag_111                                   | SAM               | 0.87995                  | 0.93290                 | 0.92899            | 0.89893             | 0.89893            |             |          |              |             |
|   | SAM2              | 0.87593                  | 0.93290                 | 0.92807            | 0.89893             | 0.89893            |             |          |              |             |
|   | MedSAM            | 0.82019                  | 0.93833                 | 0.92629            | 0.89893             | 0.89893            |             |          |              |             |
|   | <b>mSkSAM2</b>    | <b>0.92530</b>           | <b>0.96315</b>          | <b>0.95989</b>     | <b>0.95989</b>      | <b>0.95989</b>     |             |          |              |             |
| Knee_3D<br>CUBE_300                                     | SAM               | 0.65253                  | 0.89575                 | 0.77414            | 0.89893             | 0.89893            |             |          |              |             |
|   | SAM2              | 0.60018                  | 0.87687                 | 0.73852            | 0.89893             | 0.89893            |             |          |              |             |
|   | MedSAM            | 0.42498                  | 0.82904                 | 0.62701            | 0.89893             | 0.89893            |             |          |              |             |
|   | <b>mSkSAM2</b>    | <b>0.92174</b>           | <b>0.98081</b>          | <b>0.95127</b>     | <b>0.95127</b>      | <b>0.95127</b>     |             |          |              |             |
| Knee_3D_CUBE<br>Undersampled_50                         | SAM               | 0.60481                  | 0.87196                 | 0.73839            | 0.89893             | 0.89893            |             |          |              |             |
|   | SAM2              | 0.56320                  | 0.87570                 | 0.71945            | 0.89893             | 0.89893            |             |          |              |             |
|   | MedSAM            | 0.41775                  | 0.81866                 | 0.61821            | 0.89893             | 0.89893            |             |          |              |             |
|   | <b>mSkSAM2</b>    | <b>0.87059</b>           | <b>0.96993</b>          | <b>0.92026</b>     | <b>0.92026</b>      | <b>0.92026</b>     |             |          |              |             |
| <b>Knee 3D DESS Research Anatomical 86</b>              |                   |                          |                         |                    |                     |                    |             |          |              |             |
| <b>Experiment</b>                                       | femoral cartilage | lateral tibial cartilage | medial tibial cartilage | patellar cartilage | lateral meniscus    | medial meniscus    | Mean Tissue |          |              |             |
| SAM   | 0.4551            | 0.7843                   | 0.7028                  | 0.7492             | 0.5484              | 0.4198             | 0.6101      |          |              |             |
| SAM2  | 0.3841            | 0.7759                   | 0.6811                  | 0.7632             | 0.6394              | 0.4981             | 0.6236      |          |              |             |
| MedSAM  | 0.0483            | 0.4979                   | 0.5811                  | 0.7099             | 0.6207              | 0.4714             | 0.4882      |          |              |             |
| mSkSAM2   | 0.9356            | 0.9414                   | 0.9313                  | 0.9361             | 0.9365              | 0.9272             | 0.9347      |          |              |             |
| <b>Knee 3D Undersampled CUBE Research Anatomical 50</b> |                   |                          |                         |                    |                     |                    |             |          |              |             |
| <b>Experiment</b>                                       | femur             | femoral cartilage        | tibia                   | tibial cartilage   | patella             | patellar cartilage | Mean Tissue |          |              |             |
| SAM   | 0.8213            | 0.4521                   | 0.8837                  | 0.5991             | 0.9109              | 0.7632             | 0.7384      |          |              |             |
| SAM2  | 0.7550            | 0.3295                   | 0.9545                  | 0.5913             | 0.9176              | 0.7689             | 0.7194      |          |              |             |
| MedSAM  | 0.7200            | 0.0435                   | 0.9313                  | 0.5159             | 0.8047              | 0.6939             | 0.6182      |          |              |             |
| mSkSAM2   | 0.9748            | 0.8509                   | 0.9730                  | 0.8617             | 0.9620              | 0.8992             | 0.9203      |          |              |             |
| <b>Thigh 2D T1ax Clinical Anatomical 50</b>             |                   |                          |                         |                    |                     |                    |             |          |              |             |
| <b>Experiment</b>                                       | subcutaneous fat  | extensors                | hamstrings              | femoral cortex     | femoral bone marrow | adductors          | sartorius   | gracilis | nerve bundle | Mean Tissue |
| SAM   | 0.7145            | 0.8441                   | 0.9091                  | 0.7863             | 0.9329              | 0.8381             | 0.9168      | 0.8075   | 0.8470       | 0.8311      |
| SAM2  | 0.7634            | 0.9383                   | 0.8584                  | 0.8215             | 0.9438              | 0.7752             | 0.9059      | 0.9018   | 0.8481       | 0.9425      |
| MedSAM  | 0.3528            | 0.7819                   | 0.7921                  | 0.3147             | 0.9037              | 0.6359             | 0.8198      | 0.7923   | 0.5951       | 0.5804      |
| mSkSAM2   | 0.8515            | 0.9637                   | 0.9414                  | 0.8906             | 0.9537              | 0.8947             | 0.9407      | 0.9420   | 0.8945       | 0.9012      |
| mixed_Muscle_SAM  | 0.8980            | 0.9669                   | 0.9512                  | 0.9022             | 0.9530              | 0.9061             | 0.9415      | 0.9433   | 0.9100       | 0.9193      |

This table presents a tiered analysis of the performance of three baseline models: SAM, SAM2, and MedSAM. The analysis focuses on results after finetuning with the complete MSK MRI dataset (mSkSAM full dataset), where both the image encoder and mask decoder were finetuned without augmentation shifts. The first tier reports mean Dice scores under the columns 'Base' and 'Fine-tuned,' with 'Base' representing baseline zero-shot performance and 'Fine-tuned' reflecting performance after mSkSAM finetuning, averaged across all class labels and MRI slices within each dataset. The second tier evaluates tissue-specific segmentation performance across SAM, SAM2, MedSAM, and mSkSAM2 for datasets containing multiple tissue types, such as cartilage, bone, muscle, and fat, to examine variability across distinct anatomical structures. The third tier offers a detailed label-level analysis for selected datasets; it examines performance across all available labels to capture the complexity and variability of specific clinical imaging tasks. Notably, in the third tier, the thigh dataset includes an additional comparison with a strategically finetuned model ('mixed\_Muscle\_SAM') that represents a potential future direction for refinement and optimization. These tiers reflect the complexity of clinical problems, from general dataset-level performance to tissue-specific segmentation and the challenges of achieving consistent accuracy across anatomically diverse and complex label sets. This approach allows for a thorough understanding of model performance across varying levels of granularity.



### *Performance by Anatomical Label and Comparative Overview of Finetuned Models*

Figure 4d and Table 1 (Supplementary Figures 2-4; Supplementary Tables S7-S9) detail the performance of finetuned models across MSK MRI datasets and reveal how segmentation success differs by anatomical region and clinical task. Assessments at the dataset, tissue-type, and label-specific levels denote distinct challenges, particularly for smaller or curved structures.

In Knee\_3D\_DESS, mskSAM2 achieved a mean Dice score of 0.9347, surpassing SAM2 (0.6236) and MedSAM (0.4882). Large, uniform labels like femoral cartilage exhibited stable performance across strategies, while smaller and curved labels, such as the lateral and medial menisci, benefitted from larger training sets but showed diminished accuracy when datasets were mixed. These findings reveal the difficulty of generalizing across anatomically complex labels.

In Thigh\_2D\_T1ax, mskSAM2 reached a mean Dice score of 0.9012, outperforming SAM2 (0.8425). Strong segmentation of muscle (Dice: 0.9365) and bone (Dice: 0.9222) drove this performance, though fat tissue segmentation (Dice: 0.8515) was more variable. This variability reflects differences in tissue thickness, contrast, and composition, intrinsic to patient populations and critical for assessing muscular atrophy and related disorders.

Single-summary metrics often obscure important label-level performance differences. Accurate individual cartilage segmentation in Knee\_3D\_DESS is essential for monitoring osteoarthritis progression, while muscle and fat segmentation in Thigh\_2D\_T1ax directly inform sarcopenia assessments. These results emphasize the potential of general-purpose models like mskSAM2 for diverse clinical applications but support the need for task-specific refinements to achieve high-impact, label-specific accuracy. A comprehensive summary of all experiments, including class-level performance, is provided in Supplementary Tables S10-S33.

### *Statistical Analysis of MRI Acquisition Parameters on Segmentation*

Hierarchical mixed-effects modeling (Figure 5a, Supplementary Tables S34–S38) examined the impact of MRI acquisition parameters on mean Dice scores across three finetuning scenarios: (i) single-dataset, (ii) mixed-dataset (grouped by anatomy, tissue type, or sequence), and (iii) comprehensive MSK-SAM training. Data normalization, sensitivity testing, and collinearity controls ensured robust and reliable results.

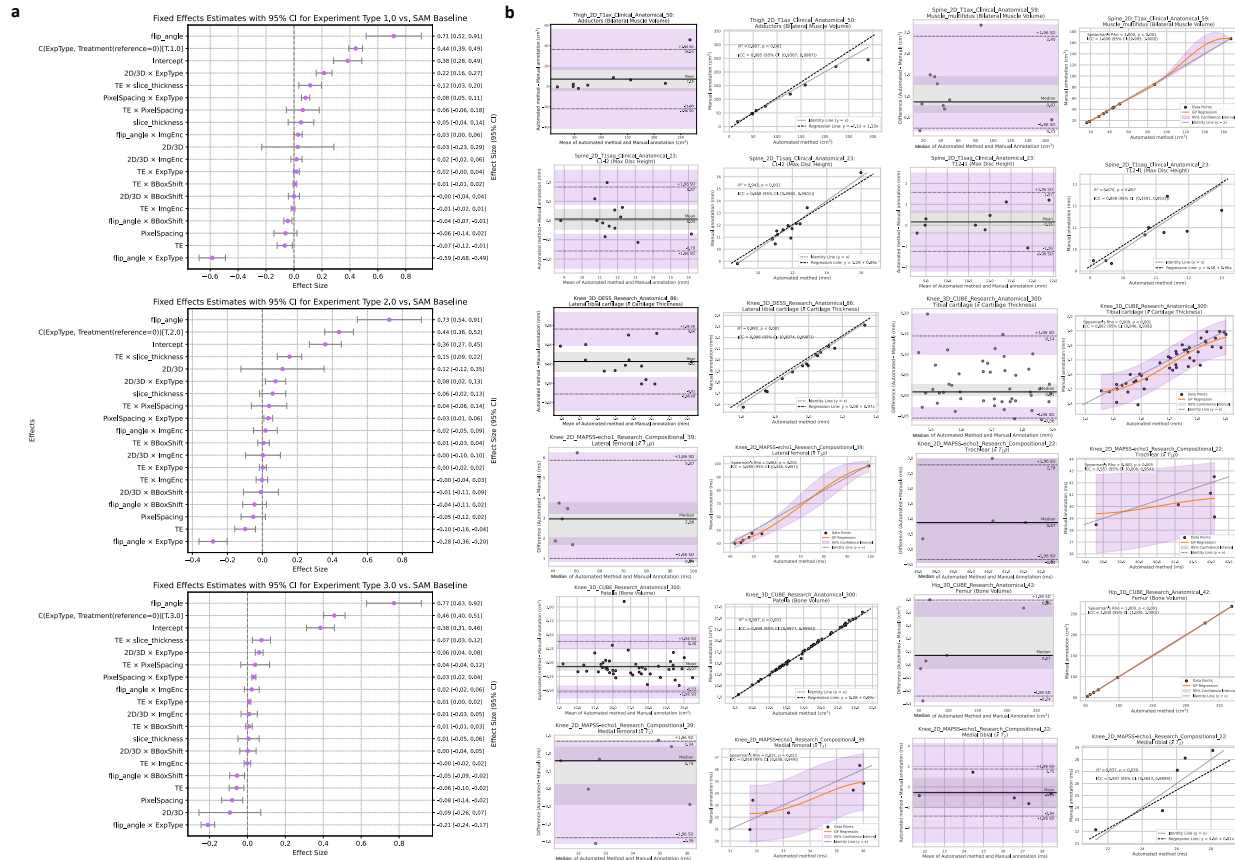
Flip angle emerged as a significant positive predictor of segmentation performance (coefficients: 0.714–0.773), reflecting its role in increasing signal intensity and contrast, which likely aids in feature delineation across MRI acquisition protocols. Conversely, echo time (TE) negatively impacted performance (coefficients:  $-0.099$  to  $-0.058$ ), with longer TE values reducing the signal-to-noise ratio (SNR) and impairing feature visibility. This effect was most pronounced in mixed-dataset training (coefficient:  $-0.099$ , 95% CI:  $[-0.158, -0.040]$ ), where diverse TE values exacerbated challenges. However, the penalty lessened in comprehensive MSK-SAM training (coefficient:  $-0.058$ , 95% CI:  $[-0.096, -0.019]$ ), suggesting broader data exposure enhances model robustness to TE variability.

The interaction between TE and slice thickness revealed a compensatory effect, where thicker slices mitigated signal loss from longer TE values by capturing more voxel-level detail. The interaction between TE and slice thickness revealed a compensatory effect, where thicker slices mitigated signal loss from longer TE values by capturing more voxel-level detail. This effect was associated with improved performance in segmenting structures requiring detailed boundary delineation, such as cartilage. Similarly, pixel spacing had a significant influence on segmentation performance (coefficient:  $-0.080$ , 95% CI:

$[-0.136, -0.025]$ ), with reduced spatial resolution associated with lower model precision in identifying anatomical structures.

These findings emphasize the importance of optimized imaging protocols for improving segmentation in clinically relevant applications. Adjusting TE and slice thickness contributed to better segmentation outcomes in structures requiring precise boundary definition. Moreover, maintaining sufficient pixel resolution contributed to greater accuracy in identifying anatomical structures. These findings suggest the importance of protocol refinements to achieve accurate and reproducible segmentation in diverse healthcare workflows.

**Figure 5: Analysis of MRI Acquisition Parameters and Segmentation Concordance in Finetuned SAM Models for Musculoskeletal MRI**



**a)** Fixed effects estimates with 95% confidence intervals (CI) for three finetuning experiment types: 1) single dataset finetuning, 2) mixed dataset finetuning based on anatomy, tissue, or MRI sequence, and 3) the comprehensive mskSAM experiment including all musculoskeletal MRI datasets. The left axis lists key MRI acquisition features (e.g., slice thickness, 2D/3D imaging, flip angle, TE time), while the right axis provides effect size estimates with 95% CI. These models assess the influence of MRI parameters on model performance, with comparisons made relative to SAM model weights as the baseline. The modeling incorporates all datasets, experiments, and model variants (SAM, SAM2, MedSAM).

**b)** Agreement between manual and automatic segmentation metrics across various biomarker measurements. Each row represents a biomarker metric (muscle volume, disc height, cartilage thickness, T1p mapping, bone volume, T2 mapping). Bland-Altman plots (left) and regression plots (right) assess concordance. For normally distributed datasets, linear regression plots show  $R^2$ , p-values, and Intraclass Correlation Coefficient (ICC3) results, while non-parametric Gaussian Process regression plots include Spearman's rho, p-values, and bootstrapped ICC results. Detailed statistical analyses are provided in the supplementary tables and figures.

## *Evaluation of Biomarker Segmentation Accuracy*

Biomarker segmentation analysis (Supplementary Tables S39–S64) demonstrated strong concordance between automated outputs from finetuned SAM models and manual expert annotations, validating their clinical relevance for measuring muscle volume, cartilage thickness, disc height, and T1 $\rho$  mapping. We feature key findings here, with comprehensive results and statistical analyses in Figure 5b and the supplementary materials (Supplementary Figures 5–10, Supplementary Tables S65–S68).

Muscle volume measurements in Thigh\_2D\_T1ax\_Clinical\_Anatomical\_50 and Spine\_2D\_T1ax\_Clinical\_Anatomical\_59 demonstrated near-perfect agreement with manual annotations. Intraclass Correlation Coefficients (ICC) ranged from 0.985 to 0.9997, with narrow confidence intervals indicating exceptional consistency. Linear regression analyses for Thigh\_2D\_T1ax yielded high coefficients of determination ( $R^2 = 0.987\text{--}0.998$ ,  $P < 0.001$ ), while Spearman's rank correlations for Spine\_2D\_T1ax were exceedingly high ( $\rho = 0.998\text{--}1.000$ ,  $P < 0.001$ ). Bland-Altman analyses revealed minimal systematic bias, with most data points lying within the 95% limits of agreement. Slight variability was observed in smaller spinal muscle groups, but overall, these results support the models' reliability for assessing sarcopenia and muscle atrophy.

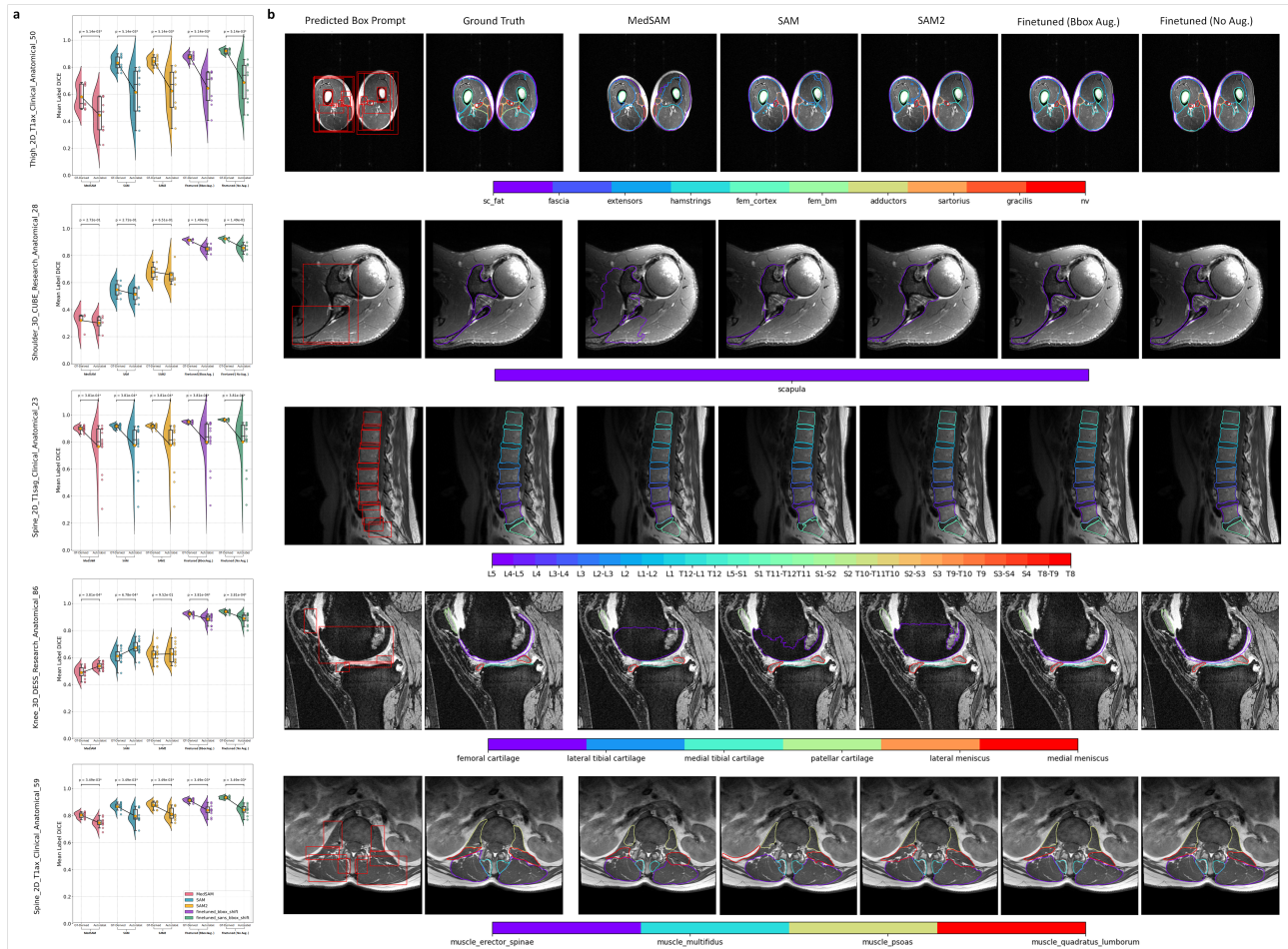
Measurements of cartilage thickness in Knee\_3D\_DESS and Knee\_3D\_CUBE datasets were highly consistent with manual annotations for femoral, tibial, and patellar regions. ICC values spanned 0.898 to 0.995, with narrow confidence intervals. Linear regression analyses showed high  $R^2$  values (0.937–0.996,  $P < 0.001$ ), and Spearman's rank correlations were comparably strong ( $\rho = 0.903\text{--}0.980$ ,  $P < 0.001$ ). The Bland-Altman plots demonstrated that the automated methods achieved reliable outcomes with minimal bias.

Disc height measurements in Spine\_2D\_T1sag\_Clinical\_Anatomical\_23 showed strong agreement with manual annotations, with ICC values of 0.808–0.971. Linear regression analyses ( $R^2: 0.670\text{--}0.943$ ,  $P < 0.001$ ) and Bland-Altman plots confirmed reliability, with minimal bias and most points within the limits of agreement. A few outliers were linked to discs with less distinct borders, validating the models' utility for assessing spinal conditions like lumbar stenosis and degenerative disc disease.

T1 $\rho$  mapping in Knee\_2D\_MAPSS-echo1\_Research\_Compositional\_39 achieved median ICC values ranging from 0.980 to 0.997, with Spearman correlations of  $\rho = 0.964$  ( $P < 0.001$ ) for the lateral femoral condyle and  $\rho = 0.893$  ( $P = 0.007$ ) for trochlear cartilage. Bland-Altman analyses revealed small median differences and acceptable limits of agreement, though patellar cartilage measurements showed some variability.

These results demonstrate the capability of finetuned SAM models to provide precise and scalable biomarker measurements. Muscle volume metrics assist in evaluating sarcopenia and guiding treatment decisions, while cartilage thickness segmentation reveals important insights into osteoarthritis progression. Disc height measurements aid in diagnosing degenerative spinal conditions, and T1 $\rho$  mapping delivers key assessments of cartilage composition. These features collectively offer value by streamlining the manual workload involved in musculoskeletal imaging and care.

**Figure 6: Comparative Performance of Segmentation Models Using Ground Truth and Automated Bounding Box Prompts Across MRI Datasets**



**a)** Raincloud plots comparing the mean Dice scores of five segmentation models (MedSAM, SAM, SAM2, Finetuned (Bbox Aug.), and Finetuned (No Aug.)) using ground truth-derived and automated bounding box prompts. Each raincloud plot combines a violin plot (showing the distribution), a strip plot with individual dots representing test subjects, and a box plot (indicating the interquartile range and median Dice score). Paired raincloud plots compare ground truth-derived prompts (left) and automated (AutoLabel) prompts from object detection (right) for each model. P-values from Wilcoxon rank-sum tests, corrected for multiple comparisons using the Benjamini-Hochberg procedure, are displayed above each paired set of raincloud plots to indicate statistical significance between the two prompt conditions.

**b)** Example segmentations from five MRI datasets (top-down): Thigh\_2D\_T1ax\_Clinical\_Anatomical\_50, Shoulder\_3D\_CUBE\_Research\_Anatomical\_28, Spine\_2D\_T1sag\_Clinical\_Anatomical\_23, Knee\_3D\_DESS\_Research\_Anatomical\_86, and Spine\_2D\_T1ax\_Clinical\_Anatomical\_59. Each dataset row shows segmentation results for MedSAM, SAM, SAM2, Finetuned (Bbox Aug.), and Finetuned (No Aug.) models. The visualizations include: (1) the original MRI slice with YOLOv8-predicted bounding boxes, (2) ground truth segmentation overlay, (3) predicted segmentation overlay, (4) ground truth contour, and (5) predicted contour. These comparisons illustrate the effect of bounding box quality, particularly the influence of automated prompts, on segmentation accuracy across diverse anatomical regions and MRI protocols.

### *Influence of Prompt Quality on Segmentation Performance*

Prompt quality emerged as a critical determinant of segmentation accuracy, with significant performance declines observed when transitioning from ground-truth bounding boxes to Autolabel-derived prompts (Figure 6, Supplementary Tables S69–S71). Dice score reductions were significant across most models ( $P < 0.01$ ), emphasizing the sensitivity of segmentation to precise bounding box generation.

SAM2 demonstrated notable robustness, maintaining stable performance in datasets such as *Shoulder\_3D\_CUBE* ( $P > 0.05$ ) despite variability introduced by Autolabel prompts. Contrastingly, finetuned models exhibited substantial Dice score reductions ( $P < 0.001$ ) in anatomically complex datasets, such as *Knee\_3D\_DESS* and *Thigh\_2D\_T1ax*, where imperfect bounding boxes often led to segmentation errors.

Figure 6 (Supplementary Figures 11–15) visually illustrates these effects, showing segmentation overlays where bounding box inaccuracies from Autolabel-derived prompts resulted in misaligned contours, particularly for smaller or more variable anatomical structures. Ground-truth prompts consistently yielded higher median Dice scores and narrower interquartile ranges, which reflects the challenges posed by prompt variability.

The Autolabel system could enable large-scale automation and dataset label transfer, proving beneficial for segmentation workflows. However, prompt inaccuracies stress the necessity of evaluating these methods in terms of their modularity, adaptability, and impact on segmentation performance. SAM2's stability with suboptimal prompts underscores its capacity for automation, though further refinement of detection methods is needed to ensure consistent and clinically applicable performance.

## **Discussion**

This study evaluates foundation models in the specialized context of musculoskeletal (MSK) MRI. Through zero-shot and finetuned paradigms, we demonstrated their potential to streamline imaging workflows and deliver precise biomarker measurements that are valuable for MSK radiological review. Our evaluation framework emphasized not only the performance of individual models but also the critical integration of modular system design, clinical contextual considerations, and focused validation strategies. This approach ensures that foundation models are assessed with a clear translational goal: to develop solutions that align with the needs of fMSK radiologists and their clinical collaborators.

SAM2 consistently outperformed SAM and MedSAM in anatomically complex regions however, none of these models were proficient for MSK MRI segmentation without domain-specific finetuning. MedSAM performed comparably in datasets characterized by more uniform label shapes, such as spinal discs, but underperformed in multifarious anatomical regions among MSK patients, like the thigh muscles and shoulder scapula. This underscores the importance of targeted refinements tailored to specific clinical needs. Finetuning experiments revealed how factors such as training set size, bounding box shift augmentation, and encoder-decoder configurations influence outcomes. Jointly training the image encoder and mask decoder without bounding box shifts proved effective, particularly in datasets with heterogeneous tissue features. Notably, Datasets with consistent anatomical structures and high-fidelity labels achieved stable performance with smaller training sets, whereas datasets with greater variability or label noise required substantially larger datasets to reach comparable accuracy.

A strength of this study is the application of hierarchical mixed-effects modeling to reveal how MRI acquisition parameters, such as flip angle, echo time (TE), slice thickness, and pixel spacing, influence segmentation performance. Higher flip angles in T1-weighted imaging enhance signal intensity and contrast, producing brighter images with sharper features, while longer TE values in T2-weighted and

proton-density-weighted datasets improve fluid visualization but may reduce signal-to-noise ratios. These findings underscore that successful adoption of foundation models into clinical workflows requires not only algorithmic advancements but also a keen understanding of the imaging physics and acquisition protocols currently embedded within the clinical ecosystem. Adjusting imaging protocols to balance TE, pixel spacing, and signal-to-noise ratios could further refine segmentation precision for clinical applications. These imaging-driven insights reinforce the value of a measured approach to model validation, ensuring clinical compatibility through strategic, purpose-driven adjustments that minimize disruption to established workflows.

Strategic mixing of datasets during finetuning proved valuable, particularly for tasks involving shared anatomical features, such as axial muscle structures in the thigh and spine. This approach facilitated feature transfer between datasets with similar anatomical and compositional details, such as knee cartilage, and enhanced performance on datasets with differing labels but shared complexities, such as bilateral thigh and spine muscle structures. By employing strategic finetuning on large or mixed datasets, segmentation accuracy improved across specific datasets while also expanding the model's generalizability to diverse imaging scenarios. This reduces the need to create new models for every use case, improves resource utilization, and supports rapid clinical deployment without extensive retraining.

This study evaluates the role of an Autolabel system in reducing the manual burden of prompt generation within medical imaging workflows. System performance was affected by inaccuracies in bounding box predictions, which degraded segmentation quality in complex three-dimensional scenarios. Refining prompting strategies to enhance accuracy remains critical. The broader objective, however, is to develop modular workflows capable of adapting to diverse prompting methods or transitioning to approaches that reduce or eliminate the need for prompting altogether. This adaptability ensures the system remains scalable and reliable as methodologies continue to evolve.

Building on these insights, the framework presented here emphasizes the need for validation strategies that prioritize clinically meaningful measures over traditional metrics like Dice and IoU. Our evaluation of finetuned models demonstrated excellent agreement with expert annotations for key MSK biomarkers such as muscle volume, cartilage thickness, disc height, and T1 $\rho$  mapping. These biomarkers provide actionable insights into diagnosing and monitoring conditions like osteoarthritis, spinal stenosis, and sarcopenia, which are central to MSK radiology workflows. By segmenting multiple tissues and extracting disease-oriented biomarkers, these models move beyond surface-level accuracy metrics to deliver outcomes directly relevant to clinical decision-making and research. Indeed, the models' precise measurements of these biomarkers reaffirm their potential usefulness in clinical research workflows.

Evaluations should extend beyond segmentation accuracy to consider data efficiency, energy consumption, and cost-effectiveness. Latent features extracted from the embedding space of finetuned models during inference encapsulate meaningful patterns learned through training, supporting broader applications such as prognostic modeling, tissue characterization, and automated quality assurance—delivering additional value without further computational costs. These features could aid in assessing tissue health, identifying early markers of disease progression, or streamlining quality control to enhance clinical efficiency and patient care. Aligning imaging protocols with the needs of both human and model interpreters ensures compatibility with existing workflows and maximizes the utility of foundation models in comprehensive medical imaging systems.

This study highlights the value of a modular, clinically focused evaluation framework for foundation models, demonstrated through MSK MRI. By aligning imaging physics, acquisition protocols, and clinical objectives, we illustrate how rigorous finetuning and validation enable these models to replace manual segmentation workflows while extracting clinically meaningful biomarkers, such as muscle volume,

cartilage thickness, and disc height. Although demonstrated in the context of MSK imaging, this evaluation strategy has potential relevance across diverse medical imaging and clinical use cases, offering a roadmap for adapting foundation models to meet specific healthcare challenges. Achieving this vision will require close collaboration among radiologists, biomedical engineers, and data scientists to ensure models meet both technical and clinical standards while remaining adaptable to evolving healthcare needs. Moving forward, interdisciplinary collaboration, data diversity, and scalable automation will be paramount to ensuring these models achieve their promise as transformative tools in medical imaging and other biomedical applications.

## Methods

### *Annotated Imaging Assets*

This study amassed diverse MRI datasets spanning various tissue types, imaging sequences, and acquisition parameters. These datasets were initially collected to investigate topics such as musculoskeletal degeneration, accelerated MRI reconstruction, and patient risk assessment; they now form a strong basis for validating methods that can streamline clinical workflows and support patient care. In addition to advancing machine learning infrastructure and evaluation frameworks, these assets promote the development of tools for diagnosing and monitoring conditions more effectively. Supplementary Table S0 summarizes dataset naming conventions, anatomical labels, and segmentation tasks; Supplementary Tables S1 and S2 provide detailed demographic characteristics and MRI acquisition parameters, respectively.

We utilized several knee MRI datasets, including the *Knee\_3D\_CUBE\_Research\_Anatomical\_300*<sup>57</sup> dataset, a high-resolution 3D fast spin echo (FSE) CUBE sequence, and the *Knee\_3D\_undersampled\_CUBE\_Research\_Anatomical\_50*<sup>57</sup> dataset, an 8x-undersampled, multi-channel k-space sequence variant of the former. These datasets, containing bone and cartilage labels, were designed to investigate the effects of accelerated MRI acquisition on downstream imaging tasks and to develop deep learning-based post-processing techniques aimed at reducing acquisition times while preserving clinical diagnostic quality. Additionally, we employed the *Knee\_2D\_MAPSS-echo1\_Research\_Compositional\_39*<sup>58</sup> and *Knee\_2D\_MAPSS-echo1\_Research\_Compositional\_22*<sup>58</sup> datasets, which support tasks such as delineating medial and lateral femoral cartilage, tibial cartilage, and the menisci. These quantitative imaging datasets enable probing of molecular and biochemical changes within cartilage associated with degenerative diseases, such as osteoarthritis<sup>35</sup>. Finally, we included the *Knee\_3D\_DESS\_Research\_Anatomical\_86*<sup>59,60</sup> dataset, derived from the Osteoarthritis Initiative (OAI) and labeled by Stryker imorphics<sup>60</sup>, which is instrumental for examining progressive structural pathology in cartilage and meniscus linked to degenerative disease.

The lumbar spine MRI datasets include several sequences: a T1 axial, a T2 axial, and two T1 sagittal sets. The *Spine\_2D\_T1ax\_Clinical\_Anatomical\_59*<sup>45</sup> dataset, labeled for muscle, was acquired to assess paraspinal muscle atrophy and fatty infiltration. The *Spine\_2D\_T2ax\_Clinical\_Anatomical\_38*<sup>45</sup> dataset, labeled for bone and cartilage, provides high-contrast imaging for examining intervertebral disc pathologies and evaluating lumbar spinal stenosis<sup>36</sup>. The *Spine\_2D\_T1sag\_Clinical\_Anatomical\_111*<sup>45</sup> and *Spine\_2D\_T1sag\_Clinical\_Anatomical\_23*<sup>45</sup> datasets, labeled for vertebral bone and cartilage, focus on segmenting vertebral bodies and intervertebral discs; the latter set offers detailed annotations from T12 to S1. Collectively, these datasets support research into spinal disorders and chronic lower back pain.

The hip dataset, *Hip\_3D\_CUBE\_Research\_Anatomical\_42*<sup>61</sup>, consists of a 3D-CUBE coronal sequence optimized to visualize the femur and surrounding tissues. This set was functional for pathophysiological research and understanding the association of bone asymmetry in hip OA<sup>62</sup>.

The shoulder dataset, *Shoulder\_3D\_CUBE\_Research\_Anatomical\_28*<sup>63</sup>, employs a 3D-CUBE sequence to capture high-resolution imaging of the scapula. This dataset was acquired to understand complex shoulder joint dynamics, with applications in orthopedic studies and surgical planning<sup>49,63</sup>.

The thigh MRI dataset, *Thigh\_2D\_T1ax\_Clinical\_Anatomical\_50*<sup>59</sup>, was acquired using a T1 axial sequence; it provides detailed segmentation of muscular anatomy and subcutaneous fat, and bone for studies focused on muscle composition and metabolic processes<sup>46-48</sup>.

Each dataset MRI sequence was configured with specific acquisition parameters such as echo time (TE), repetition time (TR), flip angles, and field strengths; these were optimized to ensure imaging protocols support reliable visualization and accurate anatomical measurements. Segmentation labels were generated through expert-annotated and semi-automated methods, providing high-fidelity information for challenging tasks. In this way, we could evaluate the segmentation models on tasks with varying levels of complexity. Such complexity includes multi-instance and multi-class labeling, irregular anatomical shapes, subject variability, and distinct imaging contrasts resulting from diverse acquisition parameters.

This study was conducted in accordance with the Declaration of Helsinki (1964) and its subsequent amendments, as well as all relevant regulations. Data acquisition and machine learning analyses were approved by the University of California, San Francisco (UCSF) Institutional Review Board (IRB), operating under Federalwide Assurance #00000068, with specific IRB approvals including 21-33865, 19-29744, 17-22581, 13-11605, and 13-11671 (data acquisition), and 18-24775 (machine learning use), respectively. The Osteoarthritis Initiative (OAI) study was conducted in accordance with IRB approvals at each OAI clinical site, including Memorial Hospital of Rhode Island, Ohio State University, University of Pittsburgh, and University of Maryland/Johns Hopkins University, with the OAI Coordinating Center at UCSF providing IRB approval (approval number 10-00532, Federalwide Assurance #00000068) and the OAI Clinical Sites Single IRB of Record approved as study number 2017H0487, Federalwide Assurance #00006378. This study is registered with ClinicalTrials.gov (identifier: NCT00080171), and an independent Observational Study Monitoring Board (OSMB) appointed by the National Institute of Arthritis and Musculoskeletal and Skin Diseases (NIAMS) oversaw adherence to ethical research standards and participant safety. All studies, including those involving UCSF data acquisition, machine learning analyses, and the OAI study, were funded by NIAMS, and all participants provided written informed consent prior to participation.

### *Model Selection and Configuration*

In this study, we evaluated three foundation segmentation models, SAM ViT-B<sup>13</sup>, MedSAM ViT-B<sup>18</sup>, and SAM2 sam2\_hiera\_base\_plus<sup>14</sup>, to assess their effectiveness in prompt-based musculoskeletal (MSK) MRI segmentation within a fully automated, scalable framework. Each model was selected based on parameter size to ensure similar computational demands for consistent evaluation. Importantly, the choice of smaller-sized models reflects both resource-conscious laboratory constraints and the practical feasibility of integrating such models into clinical pipelines. The evaluation was designed with robust yet lightweight configurations to account for healthcare-specific hardware limitations, promoting scalability and real-world usability.

### *Segment Anything Model (SAM) ViT-B*

The Segment Anything Model (SAM)<sup>13</sup> with the ViT-B encoder, with approximately 91 million parameters, was chosen for its balance of performance and computational efficiency. Trained on over 1 billion natural image-mask pairs, SAM integrates an image encoder, a prompt encoder, and a mask decoder to support promptable segmentation across various imaging tasks. The choice of the ViT-B variant ensured



compatibility with available computational resources, and provides a valuable baseline for general-purpose segmentation.

#### *MedSAM ViT-B for Medical Imaging*

The MedSAM ViT-B model is a finetuned version of SAM, specifically adapted for medical imaging. Trained on over 1.5 million medical image-mask pairs across multiple modalities and anatomical regions, MedSAM<sup>18</sup> was designed to improve segmentation accuracy in healthcare-related tasks. MedSAM retains SAM's prompt-based structure, allowing efficient clinical segmentation comparisons without additional computational requirements.

#### *SAM2 sam2\_hiera\_base\_plus*

The SAM2 sam2\_hiera\_base\_plus model extends SAM's capabilities, incorporating a hierarchical, multi-scale encoder designed for image and video segmentation with approximately 80.8 million parameters. SAM2<sup>14</sup> was trained on the expansive SA-V dataset, which includes 50,900 videos, 642,600 masklets, and over 35 million individual masks, offering broad exposure to a range of video segmentation scenarios. While SAM2 is equipped with a memory module to maintain context across frames, we limited its use to 2D prompts in this study. This approach allows prompt-based segmentation in individual MRI slices without additional spatial context, reinforcing a consistent comparison with SAM and MedSAM.

#### *Uniform 2D Prompt Configuration for MRI Segmentation*

Each model was evaluated using 2D prompts across sequential MRI slices; this configuration was, therefore, integrated into the design for our auto labeling objective. This uniformity mitigates the limitations of prompt-based systems in 3D imaging, where anatomical regions can occlude, exit, or reappear across slices. By standardizing prompt consistency across all models, we concentrated on segmentation quality driven by data and anatomy rather than model-specific interactions, providing a robust basis for assessing each model's capability in high-throughput MSK segmentation.

#### *Rationale for 2D Prompt Configuration of SAM2*

We did not activate SAM2's memory encoder for 3D MRI volumes due to inherent limitations in processing extended, slice-rich volumes. The memory module of SAM2, designed for short sequence videos, maintains frame context but faces reliability challenges with long, high-resolution sequences typical of MSK MRI. In prolonged sequences, anatomical labels often become occluded, exit, or new structures enter the field of view, requiring repeated manual prompts to continue tracking specific structures; this repeated intervention disrupts the automation valuable for clinical research. Additionally, variations across patients (e.g., differences in age, body mass index, and sex) complicate SAM2's ability to consistently track anatomical features without manual intervention.

Implementing SAM2 in a 2D context allowed for a controlled segmentation workflow that scales to multiple MRI volumes and accommodates anatomical variability without manual inputs. This approach bolsters the development of a scalable, fully automated pipeline, demonstrating the utility of SAM- and SAM2-based models in clinically realistic, high-throughput settings.

#### *Preprocessing Strategy for Model Compatibility*

We standardized the preprocessing of our MRI images and segmentation masks in order to ensure compatibility with the deep learning architectures. This approach facilitated the consistent formatting required for training and evaluating the SAM, SAM2, and MedSAM models. In addition to technical

consistency, the standardization process aimed to produce clinically useful outputs by maintaining consistent orientation and slice ordering, fundamental for follow-up imaging. Moreover, intensity normalization was implemented to aid consistent biomarker extraction and to bolster the reliability of diagnostic assessments.

### *Standardizing Medical Imaging Data Formats*

The medical imaging data used in this study originated from diverse sources and were provided in various formats, including DICOM, NIfTI, NPZ, HDF5, and MATLAB files. This diversity reflects the inherent variability of medical imaging workflows; data format selection is influenced by the tools and software employed, as well as the specific objectives of each originating study. Segmentation masks were similarly diverse, sometimes stored as separate files per label or aggregated into multi-class volumes, with formats tailored to specific downstream analyses. Furthermore, a number of datasets contained DICOM files that were rich in metadata, whereas others did not due to previous reformatting.

To address this complexity and build reproducible, scalable pipelines, all data were converted to the NIfTI (.nii) format, a widely supported standard compatible with most open-source medical imaging tools. The conversion process addressed the challenges presented by various data configurations, including 2D slices, 3D volumes, and incongruous combinations of the two. Harmonizing data dimensionality (e.g., converting 2D masks to 3D volumes) and resolving differences in mask label structures, such as combining separate class-specific files into unified multi-class volumes, ensured compact storage without losing label-specific details.

Python libraries, including nibabel<sup>64</sup>, SimpleITK<sup>65</sup>, and pydicom<sup>66</sup>, enabled the automation of these workflows while preserving essential metadata. Achieving anatomical consistency across datasets required careful alignment of orientation and slice order using metadata from DICOM files where available; when orientation information was missing, systematic checks confirmed uniform axes and spatial integrity. This consistency across datasets made additional preprocessing steps efficient with the use of a singular pipeline.

Transitioning legacy data formats to a single standard required significant upfront effort, but it established a workflow that is both efficient and reproducible. Using NIfTI simplifies future integration with computational tools and maintains dataset compatibility with evolving technologies. This process supports the broader research intention of creating transparent, interoperable, and resource-efficient medical imaging pipelines.

### *MRI Image Preprocessing Workflow*

Each 3D MRI volume was first clipped to retain pixel intensity values between the 1st and 99th percentiles of non-zero pixels. This clipping reduced the influence of outliers and enhanced robustness to intensity variations while preserving clinically relevant contrast. The images were then normalized to a range of 0 to 255 and converted to 8-bit integers. Subsequently, each 2D slice was resized to 1024×1024 pixels using cubic spline interpolation to maintain image quality. To meet the input requirements of the pretrained models, each slice was scaled to a range of 0-1 and replicated across three channels to simulate RGB input. The processed slices were saved as NumPy arrays in .npy format; this was a design choice that originated from the MedSAM study, selected for its benefits of efficient data loading and compatibility with the deep learning frameworks used.

### *Segmentation Mask Preprocessing*

The segmentation masks underwent a similar preprocessing pipeline in order to align with their associated images. Starting from 3D mask volumes, we removed unnecessary labels corresponding to anatomical

regions or features irrelevant to the study objectives. Small structures considered as noise rather than meaningful anatomy were excluded based on voxel count thresholds—objects under 100 pixels in 2D slices and under 1,000 voxels in 3D volumes. This exclusion removed artifacts and reduced the likelihood of false positives during training. Each mask slice was then resized to 1024×1024 pixels using nearest-neighbor interpolation, preserving label integrity. Masks were saved as single-channel .npy files for compatibility with the segmentation models.

### *Optional Low-Resolution Workflow for System Optimization*

For users aiming to streamline the finetuning process, preprocessing masks at 256×256 pixels instead of 1024×1024 can help reduce computational overhead. The SAM and SAM2 models inherently output lower-resolution mask logits at 256×256, and maintaining this resolution for ground truth masks allows for direct comparison during loss and metric computation, bypassing the need for upscaling. Bounding boxes generated from 256×256 masks can be scaled to align with the 1024×1024 input images, ensuring compatibility with the models. This is an optional approach to improve computational efficiency during finetuning.

A practical consideration for adopting this workflow is its impact on the broader image processing pipeline. Users should weigh the trade-offs between storage requirements for larger datasets, the potential time saved during finetuning, and the usability of the processed data for downstream analyses or future model training. For medical imaging workflows, particularly in resource-limited environments, optimizing the entire system design to balance computational, storage, and operational constraints is critical for scalability and long-term utility.

### *Adapting Data for Object Detection Models*

To adapt the data for object detection models like YOLOv8, bounding box annotations were generated directly from the ground truth segmentation masks, with coordinates normalized to the image size. These annotations were saved in .txt files in such a way that they could be paired with their corresponding .npy images. This preprocessing pipeline prepared the data for both detection and segmentation models, which supports their use as standalone systems or as part of an integrated labeling framework.

### *Technical Implementation of Preprocessing*

Custom scripts automated the preprocessing workflow, beginning with standardized NIfTI 3D volumes and further converting them into 2D slices formatted as .npy files, compatible with both segmentation and detection models. Key steps included clipping, normalization, resizing, and channel expansion for images, as well as label management and noise exclusion for masks. Bounding boxes were generated from segmentation masks to facilitate prompt-based learning in the SAM-based models and to provide annotations for the detection models. Our preprocessing pipeline was configurable; adjustments to parameters such as voxel thresholds and image dimensions could be performed as needed. In this way, the system offers flexibility to adapt to different computational resources and experimental goals.

### *Dataset Partitioning for Balanced Representation*

We partitioned each dataset into training, validation, and testing subsets using fixed ratios of 70%, 15%, and 15%, respectively. Subject splits were stratified by sex, a demographic variable shared across all datasets, to maintain balanced representation across experiments. Additionally, the pipeline can balance splits using additional variables, such as age, BMI, or clinical outcomes, which is adaptive for unique study objectives.

## *Data and Experiment Management for Baselines, Finetuning, and Evaluation*

We developed a modular pipeline to accommodate our study design which necessitates large-scale finetuning and evaluation of SAM-based models on our MSK MRI datasets. The system incorporates metadata management, standardized configuration templates, and adjustable YAML parameters to run diverse experiments at scale. Additionally, the system includes experiment tracking and model checkpointing to support a precise and reproducible workflow. These practices also facilitate clinically valid comparisons by ensuring balanced representation of diverse patient populations and scanning protocols; they enable reliable assessments that align with future clinical translation, reproducibility, and regulatory requirements.

### *Metadata Creation and Standardization*

Imaging acquisition and experimental attributes were systematically recorded through the design of comprehensive metadata that captured constructive details at both the slice and subject levels.

At the slice level, metadata included spatial properties extracted from DICOM headers, such as pixel spacing, slice thickness, and the anatomical location within the volume. Unique identifiers, including AccessionNumber and SOPInstanceUID, were incorporated to establish traceability to the original imaging data. The spatial integrity of the data was maintained throughout metric computation with use of these slice-specific metadata elements, resulting in high-fidelity downstream volumetric analyses.

Subject-level metadata included demographic and MRI acquisition parameters, including age, sex, field strength, sequence type, as well as training, validation, and testing dataset splits. Because of the balanced and repeatable dataset partitions made possible by this methodical tracking, anatomical and demographic diversity could be consistently represented across experiments. In order to maintain uniformity in data handling and analysis, the structured approach also made it possible to incorporate dataset-specific variations into the experimental workflow with ease.

Slice and subject metadata were directly linked to standardized Parquet tables that arranged paths to preprocessed images and segmentation masks. Even when working with high-resolution, multi-slice MRI volumes, this structure shortened data access times and facilitated quick training and assessment in a variety of experimental configurations.

These metadata components cooperated during evaluation and finetuning to expedite data processing and ensure reproducibility in dataset splits. Each experimental setup relied on this metadata framework to ensure that the pipeline achieved our overarching objectives of consistent and transparent data preparation. Moreover, this infrastructure ensured that all results were reproducible and traceable for further analysis, in addition to improving experiment scalability.

### *Configuration Management for Dataset Preparation and Experiment Initialization*

A specific YAML configuration template that balanced standardization with adaptability for experiment-specific modifications was used to manage each dataset; these templates specified dataset paths, imaging parameters (e.g., pixel spacing, slice thickness), and metadata references, ensuring uniform preparation across datasets. Likewise, an experiment-specific configuration template contained hyperparameters, dataset composition, and training parameters. This modularity provided a structured approach to managing the intricacy of experiments involving mixed datasets. Indeed, this framework supported a variety of experimental objectives while facilitating the systematic and repeatable preparation of data.

Model weights, GPU settings, and dataset-specific metadata were among the important parameters that were dynamically loaded during experiment initialization. Additional details about the computational resources and GPU setups can be found in the Supplementary Information – Computational Resources. Resources and parameters were seamlessly integrated into the pipeline via this dynamic loading. The automatic configuration supported both single-GPU and distributed GPU processing.

Additionally, the YAML configuration files contained parameters specific to the experiment, such as batch size, learning rate, optimizer type, scheduler configurations, and early stopping criteria. These settings were kept constant across experiments, except where the scheduler adjusted the learning rate, to provide a stable baseline while other factors were systematically varied. The pipeline simplified experiment initialization and execution by directly embedding these variables into the YAML templates; in this way our system ensured reproducibility and comparability under a variety of experimental circumstances.

### *Experiment Organization and Documentation*

To promote reproducibility and well-organized documentation, we established a systematic directory structure. The experiments were labeled with task descriptions (e.g., "mskSAM," "OAI\_Knee") and included subdirectories (e.g., "Run\_1," "Run\_2") for multiple iterations. This automated directory structure streamlined navigation and established a consistent framework for comparing experimental iterations.

Comprehensive experiment logging was implemented to ensure reproducibility and adherence to high documentation standards. When integrated with Weights & Biases (W&B)<sup>67</sup>, the system recorded detailed metrics, including learning rates, batch sizes, optimizer and scheduler configurations, gradient accumulation settings, and Dice similarity coefficients computed using the MONAI<sup>68</sup> library. The system was also built to accommodate non-W&B integrated workflows; numerical data for training and validation loss values and Dice coefficients were saved in JSON-format, and visualizations saved as PNG files to the local experiment run directory.

To verify data integrity and monitor model performance during early stages of training, optional quality control visualizations were included. These visualizations displayed inputs, bounding box prompts, ground truth masks, and predictions during initial epochs. These visual aids, saved within associated experiment directories, helped validate the preprocessing and augmentation steps, as well as offer real-time feedback on the behavior of the model.

### *Model Checkpointing for Finetuning and Inference*

A consistent checkpointing system was implemented to enable seamless reloading of finetuned models for continued finetuning, evaluation, or inference. During distributed training, PyTorch's<sup>69</sup> Distributed Data Parallel (DDP) framework adds prefixes (e.g., model.) to parameter keys in the state dictionary to reflect the distributed wrapper. At the end of each finetuning run, an automated conversion procedure was used to address this, eliminating these prefixes and returning the state dictionary to its initial configuration. This ensured compatibility with SAM and SAM2 systems, enabling checkpoints to be seamlessly reloaded across single- and multi-GPU environments; checkpoint paths were automatically recorded for reproducibility.

### *Dataset Summaries and Experiment Snapshots*

Each experiment's YAML configuration file was saved as a text snapshot inside the experiment directory to preserve transparency and make replication easier in the future. This immutable record preserved all hyperparameters, model specifications, and training settings. Additionally, dataset characteristics were recorded in a CSV file summarizing key statistics, including the total number of subjects, training-

validation-test split counts, number of slices, processed slices, and average demographic information. The comprehensive overview of the data used in this programmatically generated summary made it simple to compare the data distributions across various experiments.

With this structured data and experiment management system in place, we implemented a unified evaluation pipeline to ensure consistent performance tracking and statistical analysis across baseline and finetuned models.

### *Evaluation Pipeline for Segmentation Metrics*

In order to assess the performance of both zero-shot baseline and finetuned models, we developed an evaluation pipeline that computes traditional segmentation metrics including the Dice similarity coefficient. This pipeline emulates the finetuning configuration by smoothly tracking evaluation runs and metrics across multiple model checkpoints. While designed with machine learning evaluation as the primary goal, the pipeline's resolution at both the subject and slice levels offers additional functionality. It can be used to track segmentation performance over time in cases of anatomical changes or disease progression, given appropriate data.

### *Configurable and Scalable Evaluation Framework*

Like the aforementioned finetuning system, we used a YAML-based configuration system for consistent organization. Different configuration files were used to identify evaluation runs; these files included preferences for model checkpoints, dataset paths, batch size, and metric tracking. Evaluation runs were systematically documented in task-specific directories. Dice metrics at the slice, subject, and dataset levels were recorded in CSV files, which provides a detailed view of model performance.

To support large-scale evaluations, the pipeline integrated with Weights & Biases (W&B) for centralized metric tracking and visualization, while also providing local logging options for flexibility. Quality control visualizations, including input images, ground truth masks, bounding box prompts, and predicted masks, were generated for each run. These visualizations made it easier to identify preprocessing errors, and supported continuous reliability tests. This transparent and reproducible monitoring enabled comprehensive analysis across multiple datasets and finetuned models.

### *Multi-Class and Multi-Instance Segmentation Workflow*

In order to address the complexity of musculoskeletal MRI datasets, the pipeline utilized a custom dataset class, `MultiClassSAM2Dataset`, engineered for multi-class and multi-instance segmentation tasks. This class generated binary masks for each segmentation label, computed bounding boxes, and addressed label inconsistencies across slices. A custom collation function was implemented to handle variability in the number of class labels and label instances across slices and subject volumes. Through the standardization of data sample batching, the function guaranteed proper formatting of images and bounding box prompts for the PyTorch pipeline. This maintained compatibility and allowed for robust processing across a variety of datasets.

During inference, the evaluation engine initialized test set data loaders using the `MultiClassSAM2Dataset` class and its collation function. Model inference and Dice score calculations were managed using the MONAI library, with class-level Dice scores computed for each segmentation label and aggregated to the subject and global dataset levels. The metrics from numerous evaluations were systematically accrued for downstream analyses and statistical evaluation.

### *Objective Metrics Without Post-Processing*

To maintain clarity and objectivity in our results, we deliberately refrained from applying post-processing techniques during evaluation. Although these techniques can differ greatly between studies and skill levels,

replicability is hampered by the insufficient detail that is commonly reported in literature. Consequently, to better understand the models' capabilities in the context of MSK MRI tasks, we assessed model performance in an unaltered state. This strategy provides consistent benchmarking with traditional segmentation metrics, and established a baseline for the more detailed evaluations conducted later in the study.

### *Baseline Model Performance and Statistical Analysis*

Using the unified evaluation pipeline, we first assessed the zero-shot segmentation performance of three models across multiple musculoskeletal MRI datasets: the Segment Anything Model (SAM), its medically adapted counterpart MedSAM, and the newer SAM2. SAM served as a general-purpose segmentation baseline, MedSAM was specifically adapted for medical imaging tasks, and SAM2, developed by Meta, extends SAM's architecture with additional training on natural images and video.

The overlap of the ground truth and predicted segmentation masks was computed using the Dice similarity coefficient. The Dice scores represent the average performance across all segmentation labels and test-set subjects within each dataset (Supplementary Table S3).

To determine whether there were significant differences in Dice scores among the three models, we applied the Friedman test, a non-parametric test suitable for repeated measures data. This test compares the ranks of the Dice scores for each subject across the three models, accounting for within-subject variability. The Friedman test is appropriate in this context because the same subjects are evaluated under multiple conditions (i.e., different models). The results of the Friedman test are presented in Supplementary Table S4.

For datasets where the Friedman test indicated statistically significant differences, we conducted post hoc pairwise comparisons using the Wilcoxon signed-rank test. This non-parametric test is suitable for comparing two related samples and assesses whether the distribution of differences between paired observations is symmetric around zero. Pairwise comparisons were performed between SAM and MedSAM, SAM and SAM2, and MedSAM and SAM2. Results of the Wilcoxon signed-rank tests, including test statistics, unadjusted p-values, and p-values adjusted using the Benjamini-Hochberg false discovery rate (FDR) correction, are reported in Supplementary Table S5. A difference in model performance was deemed statistically significant if the corrected p-value was less than the significance threshold ( $\alpha = 0.05$ ).

Fig. 3a shows box-and-whisker plots of Dice score distributions for each model on musculoskeletal MRI datasets, highlighting the median, interquartile range (IQR), and outliers, while Fig. 3b displays variance plots, illustrating the consistency of model performance across said datasets. The results of the baseline analysis provided an understanding of the general proficiency of SAM, MedSAM, and SAM2 to function in a medical imaging scope, and served as a reference for assessing model performance across subsequent finetuning strategies.

### *Finetuning Strategies, Model Ablation, and Dataset Mixing*

We investigated several configurations of SAM-based models, SAM, MedSAM, and SAM2, across several musculoskeletal MRI datasets in order to thoroughly assess the impact of various finetuning techniques on segmentation performance and computational efficiency. These finetuning methods were designed to improve segmentation accuracy, with potential to streamline clinical interpretation; reliable results can enhance patient assessment and reduce the manual workload for MSK radiologists. Supplementary Table S6 specifies the dataset combinations and configurations within these experiments, linking named experiments to the anatomical regions and dataset types used. Our objective was to identify the optimal strategies for musculoskeletal MRI segmentation tasks.

### *Data Preparation for Finetuning*

As outlined in the earlier preprocessing strategy, the pipeline was applied consistently across datasets to ensure compatibility with the finetuning process while maintaining computational efficiency. Such standardization supports rapid finetuning for experimental validation, and demonstrates the adaptability needed to manage dynamic datasets and imaging protocols, should the system be deployed and maintained in clinical settings.

### *Training Hyperparameters and Regularization*

Our training configurations were optimized to balance computational feasibility and model performance in order to ensure consistency across finetuning experiments. The AdamW<sup>70</sup> optimizer, with a learning rate of 0.0001 and weight decay of 0.01, was chosen to ensure robust convergence and effective regularization. A CosineAnnealingWarmRestarts<sup>71</sup> scheduler dynamically adjusted the learning rate, enhancing the model's ability to escape local minima. Regularization techniques, including early stopping after ten epochs of no validation loss improvement (minimum delta 0.0001) and gradient clipping with a maximum norm of 1.0, were applied to stabilize training. Stable convergence is essential for clinical workflow applications, where irregular model outputs could mislead radiological interpretations. Thus, early stopping and gradient clipping were employed to prevent inconsistent results that could undermine the reliability of model outputs in potential patient assessments. Gradient accumulation over four steps allowed effective scaling of batch sizes while adhering to memory constraints, with a batch size of two chosen to maximize training throughput. Mixed-precision training with CUDA<sup>72</sup> Amp was employed to reduce memory usage without compromising performance. The loss function combined Dice Loss with Binary Cross-Entropy with Logits Loss (BCEWithLogitsLoss), leveraging sigmoid activation to maintain compatibility across diverse segmentation tasks in musculoskeletal MRI datasets while ensuring efficient backpropagation.

### *Model Architecture Ablation Experiments*

To evaluate the trade-offs between segmentation performance and computational efficiency, we conducted model architecture ablation experiments focusing on the SAM architecture. This model comprises an image encoder that extracts feature representations, a mask decoder that generates segmentation masks from embeddings, and a prompt encoder that transforms bounding box prompts into embeddings for the mask decoder. This modular design allowed us to selectively finetune specific components by adjusting the training configurations.

We investigated two primary finetuning strategies: (i) Full Finetuning, where we updated both the image encoder and the mask decoder during training, and (ii) Partial Finetuning, where we trained only the mask decoder while keeping the image encoder frozen. Full Finetuning, though computationally intensive, may yield significant improvements given the differences between SAM's original natural image training data and the medical imaging domain. Partial Finetuning, in contrast, offers memory efficiency and may enable the incorporation of more resource-intensive protocols, such as advanced augmentations or larger batch sizes, for certain datasets. Although these specific protocols were beyond the scope of this study, their potential benefits informed the design of our experiments.

While full finetuning can boost accuracy, partial finetuning may suit clinical settings where computational resources are restricted, thereby enabling more sites to implement automated segmentation without major infrastructure upgrades. By comparing these strategies, we aimed to determine whether the computational demands of Full Finetuning justify potential performance gains or whether Partial Finetuning suffices for musculoskeletal MRI segmentation tasks.

### *Bounding Box Prompt Shift Augmentation*

The training procedure was modified to include bounding box prompt shift augmentation in an attempt to increase the resilience and generalizability of the model; this method entailed applying random perturbations, with a shift magnitude of 20 pixels, to the bounding box coordinates obtained from ground



truth segmentation masks. Through the emulation of realistic bounding box misalignments, this approach addresses the variability inherent in clinical workflows, where minor errors introduced by staff or automated tools can occur. We implemented this approach in order to test the models' capacity to extrapolate to conditions with imprecisely aligned prompt inputs and inconsistencies in clinical research.

#### *Dataset Mixing for Enhanced Generalization*

To explore strategies for optimizing generalization in resource-constrained medical imaging settings, we included both single-dataset and multi-dataset configurations in our finetuning experiments. We sought to overcome the limitations of small or insufficient datasets by combining datasets with complementary attributes. This approach reflects a practical challenge in medical imaging: datasets are often curated for specific studies, yet their strategic combination may yield broader utility for new tasks. This approach recreates conditions in which multiple imaging centers depend on various scanners and protocols and represents the variability common in multi-hospital settings. Improved generalization from these experiments can support consistent biomarker extraction and segmentation performance across diverse patient populations. By mixing datasets based on anatomy, MRI sequence, and segmentation task similarity, we evaluated whether broader finetuning on related datasets could establish a strong foundation for subsequent finetuning on more targeted datasets with minimal computational overhead.

For anatomy-specific groupings, we focused on the knee and spine datasets. The knee group included MAPSS echo1, 3D DESS, and 3D CUBE sequences with varying resolutions and segmentation complexities. Finetuning on this mixed dataset aimed to create a robust knee-specific model capable of generalizing across different MRI sequences and tasks, such as bone, cartilage, and meniscus delineation. The spine group combined T1 axial, T1 sagittal, and T2 axial sequences to explore whether segmentation performance for spinal structures could be enhanced by training on mixed MRI sequences and orientations. This setup assessed if a spine-specific model could leverage additional contextual information provided by multiple imaging planes.

In addition to anatomy-focused groupings, we created a muscle-focused dataset by combining the T1 axial thigh and T1 axial spine muscle datasets. Despite differences in anatomical regions, these datasets share similar imaging characteristics, such as bilateral muscle visibility in axial orientation. This combination investigated whether leveraging similar tissue structures and orientations could improve segmentation accuracy, particularly when individual datasets were small. The most extensive combination, mskSAM, included all available MRI datasets, excluding the 8×-undersampled knee CUBE sequence reserved for validation purposes. This mix strove to determine whether exposure to a wide range of anatomical regions, MRI sequences, and segmentation tasks could enhance the generalizability of SAM-derived models across diverse clinical scenarios in musculoskeletal imaging.

#### *Data Ablation Strategy for Resource-Limited Scenarios*

To simulate varying levels of data availability and assess model stability under limited data conditions, we applied a data ablation strategy for each single- and multi-dataset experiment. We tested training set sizes of 5, 10, 20, and 40 subjects per dataset within a group. Prioritizing subject counts over raw data volume maintained consistency across datasets and prevented imbalances due to varying slice counts and resolutions inherent in musculoskeletal MRI studies. Clinics often encounter specialized MSK pathologies with limited data. Evaluating performance under these constraints helps ensure that our pipeline can still provide accurate segmentations for rare or understudied conditions. In cases where a dataset lacked sufficient subjects to meet the designated training size, we included the maximum available subjects while other datasets contributed up to the specified limit. This approach evaluated the model's capacity to adapt and generalize under varying dataset size conditions, across both single- and mixed-dataset configurations, within the context of musculoskeletal MRI data.

#### *Integrated Ablation Analysis and Clinical Relevance*

In addressing clinically relevant challenges in musculoskeletal imaging, we conducted an integrated ablation analysis combining model architecture ablation, data ablation, and bounding box shift augmentation experiments, focusing on the SAM model. These experiments examined the effects of bounding box shift augmentation on model adaptability, as well as the relative merits of full versus partial finetuning across varying dataset sizes and conditions. By testing these strategies in parallel and combination, we explored scalable solutions for clinical settings where dataset availability and homogeneity are often constrained.

Given the extensive resource requirements of such thorough analyses, we prioritized SAM due to its foundational role in subsequent SAM-based models, MedSAM and SAM2. This focus allowed us to establish baseline strategies for optimizing SAM architecture under varying constraints, providing actionable insights into model adaptability and scalability. While MedSAM and SAM2 were not subjected to the full scope of these experiments, the consistent SAM-derived architecture positions these insights as a practical guide for designing their finetuning workflows in resource-constrained environments.

Our finetuning strategies and dataset mixing were further designed to examine whether combining datasets could compensate for dataset-specific limitations and improve the model's ability to generalize structural details of musculoskeletal anatomy, such as tissue boundaries, spatial relationships, and shape variability. These ablation analyses were combined to identify configurations suitable for radiology workflows; the intention is to reduce reliance on specialized hardware or extensive data while achieving accurate and clinically relevant segmentations. This method reflects practical challenges in clinical imaging research, where datasets are often diverse but constrained by small sample sizes, narrow task focus, or variability in imaging protocols. Supplementary Tables S7 and S8 provide additional insights into finetuning configurations and tissue-specific segmentation performance, supporting the evaluation of SAM-derived models across these mixed and ablated settings. By evaluating these strategies, we aimed to provide a framework for optimizing segmentation models that balance scalability, adaptability, and anatomical specificity in musculoskeletal MRI.

#### *Impact of Initial Weights on Model Finetuning Performance*

Building upon our finetuning strategies developed for this study, we further investigated how different initial weights influence the finetuning performance of SAM-based models in musculoskeletal MRI segmentation tasks. The choice of initial weights can significantly affect model convergence, performance, and generalization, particularly in specialized domains like medical imaging. To this end, we conducted a systematic evaluation of baseline weights derived from the original SAM, MedSAM, and SAM2 models.

Each of these models was pretrained on distinct datasets: SAM on a vast collection of natural image-mask pairs, MedSAM on a smaller but diverse set of medical image-mask pairs across multiple modalities, and SAM2 on a combined dataset of natural images and video sequences enriched with mask annotations. By applying both Full and Partial Finetuning, we aimed to assess whether the choice of initial weights conferred distinct advantages based on dataset characteristics and segmentation tasks.

We conducted this analysis on several musculoskeletal MRI datasets, such as those from the knee, spine, shoulder, and thigh, each of which covered a range of imaging properties and segmentation task complexity. This method allowed us to systematically examine how initial weights and finetuning techniques interact to improve segmentation performance. Supplementary Table S9 summarizes baseline weight performance in the mskSAM finetuning configuration, highlighting potential candidates for musculoskeletal MRI segmentation foundation models.

In addition to single-dataset experiments, we included the comprehensive mskSAM finetuning configuration that encompassed all available datasets. This enabled us to explore the potential of each set of initial weights to serve as a foundation for generalizable musculoskeletal MRI segmentation models

capable of handling diverse anatomical regions and imaging modalities. A detailed summary of class-level performance metrics for each segmentation task and experiment is provided in Supplementary Tables S10-S33.

In order to isolate the impact of initial weights on performance variations and make sure they reflected compatibility with the data properties, we maintained consistent finetuning protocols. This assessment provides recommendations for choosing sensible starting points for optimizing SAM-based models in medical imaging and highlights the need for flexible, iterative validation systems. Such systems will enable rapid evaluation of newly finetuned weights and help determine whether they should replace existing models in response to evolving patient data or clinical needs. Supporting continuous adaptation ensures that this approach allows future models to remain reliable and scalable, irrespective of changes in data distribution.

### *Preprocessing and Hierarchical Mixed-Effects Modeling of Imaging Parameters and Finetuning Strategies*

Following the completion of all finetuning experiments, we carried out a thorough statistical analysis to assess how MRI parameters<sup>23</sup> and finetuning techniques affected model performance. We employed hierarchical mixed-effects modeling to rigorously assess how different imaging and experimental factors influenced the mean Dice similarity coefficient across subjects, allowing for in-depth comparisons relative to the SAM baseline. Examining performance variations in relation to MRI-specific parameters provides a way to better understand how imaging protocols and experimental configurations influence segmentation outcomes. This analysis encourages deeper consideration of medical imaging ecosystem design, particularly if models like SAM demonstrate value for integration into clinical workflows; any protocol adjustments informed by this analysis could have broader implications for the overall imaging system.

### *Data Preprocessing for Mixed-Effects Modeling*

Our dataset, as presented in Supplementary Tables S34 and S35, underwent a detailed preprocessing routine to ensure it was suited for hierarchical mixed-effects modeling. The goal of this procedure was to standardize numerical variables, handle missing values, and encode categorical variables in order to give a reliable basis for precisely assessing how MRI parameters affect segmentation accuracy and optimizing strategies. The imputation and transformation steps were carried out twice: once before conducting feature selection using Variance Inflation Factor (VIF) analysis and again after the removal of highly collinear features.

Variables were categorized by type, and missing values were handled using specific approaches suited to each type. Specifically, for categorical nominal variables, missing values were imputed using a Random Forest Classifier implemented in scikit-learn<sup>73</sup>, selected for its ability to capture complex interactions among variables. These nominal variables were then one-hot encoded, with the first category omitted to avoid introducing multicollinearity. Additionally, categorical ordinal variables were ordinally encoded to retain their inherent order; missing values were similarly imputed using a Random Forest Classifier. These ordinal variables were transformed into integers that reflected their hierarchical rank.

Continuous numerical variables were treated with an iterative imputation method using a Random Forest Regressor, preserving the natural relationships and distributions in the data. After imputation, these variables were standardized with the StandardScaler from scikit-learn to achieve a mean of 0 and a standard deviation of 1. Discrete numerical variables, such as "FlipAngle" and "ImageRowSize," were also imputed using a Random Forest Classifier to maintain their discrete properties. Certain discrete variables, including

"Age," "FlipAngle," and "ImageRowSize," were then normalized using the MinMaxScaler to confine values within a 0 to 1 range.

To confirm that the imputation process preserved the data's original characteristics, we conducted a sensitivity analysis using the Kolmogorov-Smirnov (KS) test, comparing original and imputed distributions. The KS test results, detailed in Supplementary Table S36, confirmed that the imputed values maintained alignment with the original data distributions.

This thorough preprocessing ensures that clinically relevant nuances in the data, such as variations in MRI scanner technology, imaging protocols, and acquisition parameters, are accurately captured. By accounting for these differences, the final analysis remains relevant to the variability encountered in radiology settings. Following imputation, scaling, and encoding, the transformed features were recombined into a cohesive dataset. This final dataset included binary-encoded categorical nominal variables, integer-encoded categorical ordinal variables, scaled continuous and discrete numerical variables, along with original identifiers and target variables. This fully processed dataset was then subjected to feature selection through VIF analysis, setting the stage for hierarchical mixed-effects modeling.

#### *Feature Selection Using Variance Inflation Factor (VIF)*

To identify and mitigate multicollinearity among features, we conducted a Variance Inflation Factor (VIF) analysis after the initial preprocessing. VIF quantifies how much the variance of a feature is inflated due to its linear correlation with other features, indicating potential multicollinearity that could distort statistical modeling results. Features with VIF values exceeding ten were deemed highly collinear and removed to reduce the risk of multicollinearity impacting the mixed-effects modeling outcomes.

We calculated VIF values for key MRI imaging features, including Echo Time (TE), Repetition Time (TR), Flip Angle, Field Strength, Scanner Vendor, Slice Thickness, Image Row Size, Pixel Spacing, Acquisition Mode (2D vs. 3D), and Specific Absorption Rate (SAR). The VIF for each feature was calculated using the formula:

$$VIF_i = \frac{1}{1 - R_i^2}$$

where  $R_i^2$  is the coefficient of determination obtained by regressing feature  $i$  on all other features. Features with VIF values above the threshold were removed, and the remaining features were re-evaluated to confirm that multicollinearity had been adequately addressed.

To finalize our dataset for the hierarchical mixed-effects modeling, we repeated the imputation, encoding, and scaling processes for the remaining variables, as detailed in Supplementary Table S37. This step creates a reliable dataset, eliminating multicollinearity to capture unbiased effects of MRI imaging parameters and finetuning strategies on segmentation performance.

#### *Hierarchical Mixed-Effects Modeling of MRI Parameters and Finetuning Strategies*

We employed hierarchical mixed-effects models to investigate the influence of MRI imaging parameters and finetuning strategies on segmentation model performance, using the mean Dice score across subjects in each dataset (MeanDiceScore) as the dependent variable. The Segment Anything Model (SAM) baseline served as the reference group for all comparisons, which allowed us to assess the effects of different finetuning strategies relative to said baseline.

The finetuning strategies used in the analysis were categorized into three types: Type 1, Type 2, and Type 3. Type 1 involved finetuning models in discrete contexts by training on individual datasets. Type 2 included training on a mix of datasets grouped by shared characteristics, such as anatomical structure, tissue type, or MRI sequence. The third type, known as mskSAM, was a thorough training strategy that made use of all available musculoskeletal MRI datasets. These strategies were applied across the SAM, MedSAM, and SAM2 models to enable a comparative analysis of finetuning effects relative to the SAM baseline.

In order to understand the influence of MRI imaging characteristics on model performance, important parameters were included in the models as fixed effects. These were Echo Time (EchoTime), pixel spacing (PixelSpacing), slice thickness (SliceThickness), and flip angle (FlipAngle). To represent the impact of acquisition dimensionality on Dice scores, a binary variable called Acquisition Mode (AcquisitionMode) was also included. It was coded as 0 for 2D acquisition and 1 for 3D acquisition.

In addition to MRI-specific variables, experimental variables relevant to the finetuning process were included as covariates to capture the influence of model architecture modifications and data augmentation techniques on segmentation performance. These covariates included Image Encoder Finetuned (ImageEncoderFineTuned), which indicated whether the image encoder component of the model was updated during training, and Bounding Box Shift Applied (BoundingBoxShiftApplied), which reflected whether bounding box shift augmentation had been employed.

We included random intercepts for every dataset in order to properly model the hierarchical nature of the data and account for the variability across datasets. The mixed-effects model was designed to capture both fixed and random effects, with a focus on exploring interactions between MRI parameters, experimental conditions, and finetuning strategies. Specifically, the model's fixed effects encompassed main effects, two-way interactions, and finetuning-specific covariates. The main effects represented the primary influence of MRI parameters (e.g., Echo Time, Pixel Spacing) and experimental conditions on Dice scores. Two-way interactions, such as those between Echo Time and finetuning strategy, were included to evaluate whether the response of Dice scores to specific MRI parameters varied according to the finetuning method used. Finetuning-specific covariates, including architectural adjustments (e.g., whether the image encoder was finetuned) and data augmentation methods (e.g., bounding box shift application), were included to examine their independent impacts on model performance.

Separate models were fitted for each finetuning strategy to provide detailed comparisons relative to the SAM baseline. Effect sizes with 95% confidence intervals were estimated for all parameters. The results of these analyses, including effect sizes and confidence intervals, are visualized in Fig. 5a, with detailed statistical outputs provided in Supplementary Table S38.

This advanced statistical method provides practical insights for incorporating SAM-based models into medical imaging workflows by reconciling computational model optimization and the complexities of MRI acquisition protocols. Connecting these statistical insights to practical considerations in radiology reveals opportunities to refine acquisition protocols and finetuning techniques. While preliminary, this analysis helps identify areas where performance optimizations could align with clinical and imaging research needs.

### *Validation of Model Performance through Clinical Biomarker Analysis*

We contrasted biomarkers derived from expert manual annotations with those generated by model-predicted segmentations to evaluate the clinical relevance and sufficiency of our segmentation models. The evaluated biomarkers included cartilage thickness<sup>38-40</sup>, T<sub>1</sub>ρ/T<sub>2</sub> mapping<sup>41-43</sup>, intervertebral disc height<sup>44,45</sup>, and muscle and bone volumes<sup>46-52</sup> all of which are significant indicators in diagnosing and monitoring musculoskeletal health. This cross-comparison spanned diverse MRI datasets and anatomical regions to

verify whether model-derived metrics align adequately with established clinical benchmarks. We sought to ascertain the accuracy and dependability of these measurements as potential substitutes for manual segmentation in medical imaging settings.

To ensure computational accuracy and alignment with imaging parameters, the pipeline integrated MRI metadata to precisely scale each metric to real-world dimensions; this supports the translation of model outputs into clinically interpretable metrics. Demonstrating the reliability of these metrics is necessary for supporting automated segmentation in radiology workflows, where accurate evaluations of cartilage, disc health, and muscle volume can improve treatment planning and follow-up care.

We performed several analyses to assess the reliability, consistency, and agreement between segmentations that were manually annotated and those that were derived from a finetuned model. These included Bland-Altman plots, regression analyses, Spearman's rank correlation, and Intraclass Correlation Coefficients (ICC), all of which were designed to identify unique relationships in the data.

Parametric methods were used when data met normality and variance homogeneity assumptions; contrastingly, non-parametric methods were applied to cases where these assumptions did not hold. In this way, this multifaceted approach thoroughly validated each model's performance and provided insights into their translational viability.

### *Evaluation Pipeline for Biomarker Comparison*

We developed a biomarker evaluation pipeline to translate segmentation model outputs into clinically interpretable metrics. The pipeline employs modular, flexible metric classes to accommodate a range of clinically relevant biomarkers, including cartilage thickness, tissue volume, intervertebral disc height, and  $T_{1\rho}/T_2$  relaxation times. Each metric class allows for calculations at the slice level and aggregation to the subject level for comprehensive dataset analysis.

The pipeline leverages MRI imaging parameters, such as pixel spacing and slice thickness, to convert pixel- or voxel-based measurements into real-world dimensions like millimeters or centimeters. Metadata files containing these parameters are referenced for each subject to align segmentation masks with the specific imaging geometry. This ensures that the computed metrics maintain both anatomical accuracy and clinical applicability.

Each biomarker is computed using methods tailored to its specific characteristics. For instance, cartilage thickness is measured via a medial axis transformation and Euclidean Distance Transform, which maps distances from the cartilage's centerline to its boundary, accommodating even irregular structures. Tissue volume is calculated through voxel counting and volume scaling, essential for accurate measurements of muscle and bone mass. Intervertebral disc height is determined by calculating the vertical extent of each segmented disc, supporting detailed spinal assessments.  $T_{1\rho}$  and  $T_2$  relaxation times, which capture the biochemical characteristics of tissues, are obtained by averaging signal intensities within segmented regions.

In order to facilitate effective downstream analysis and cross experiment comparisons, the pipeline stores calculated metric results in standardized CSV files. The evaluation runs are primarily organized by YAML configuration files, which specify parameters like the chosen biomarkers, relevant mask tissue labels, and metadata required for scale conversion. This design offers a scalable approach for biomarker analysis in musculoskeletal MRI studies, which enables parameter modifications while preserving standardization of metadata and scaling across various datasets. Such a standardized approach is advantageous in clinical and

research contexts, where radiologists and researchers may need streamlined methods for comparing data across multiple institutions or for tracking patient outcomes over time.

### *Cartilage Thickness Evaluation*

To assess cartilage integrity in key anatomical regions of the knee—specifically the femur, tibia, and patella—we computed cartilage thickness using a post-processing pipeline that applies the medial axis transformation<sup>73</sup> and the Euclidean Distance Transform<sup>74</sup> (EDT). The medial axis transformation extracts the central skeleton of the cartilage regions from the segmentation masks. Thickness is then calculated by measuring the Euclidean distance from each skeletal point to the nearest boundary pixel using the EDT. These distances, representing cartilage thickness, are scaled according to the MRI voxel dimensions to obtain anatomically accurate measurements in millimeters.

Both the predicted cartilage masks (from the model) and the ground truth masks (from manual annotations) underwent this transformation for each MRI slice. Mean cartilage thickness was determined by averaging thickness values along the cartilage skeleton within each region of interest. This process was performed across all relevant tissue labels, and results were aggregated across slices to produce subject-level summaries of cartilage thickness.

By calculating cartilage thickness along the centerline, this method captures the structure's entire geometry; medial axis transformation and EDT provide a consistent approach to measuring thickness, even in irregular or deformed regions. Because small reductions in cartilage thickness can signal early degenerative changes, consistent automated measurements may enable earlier clinical interventions for conditions like osteoarthritis, promoting better patient outcomes. The resulting metrics provided a quantitative basis for evaluating model performance against manual annotations, serving as a foundation for statistical analyses of agreement and consistency. This technique also illustrates how the resulting metric could be applied to evaluate the structural health of cartilage in both clinical and research settings.

### *T<sub>1ρ</sub> and T<sub>2</sub> Relaxation Time Mapping*

T<sub>1ρ</sub> and T<sub>2</sub> relaxation times are valuable for analyzing the biochemical composition and health of cartilage, particularly for detecting early degenerative changes such as proteoglycan depletion and collagen network disruption. Calculating these values from both model-predicted and manual segmentations provided insights into the model's ability to emulate manual annotations in revealing subtle biochemical variations. A well-functioning automated segmentation system has the potential to support the use of T<sub>1ρ</sub> and T<sub>2</sub> biomarkers to monitor cartilage health and assess therapy effectiveness.

For each MRI slice, we extracted T<sub>1ρ</sub> or T<sub>2</sub> relaxation time values within the segmented cartilage regions by applying the predicted and ground truth segmentation masks to the corresponding relaxation time maps. The relaxation time values within each segmented region were averaged to generate a representative value for each anatomical compartment, including the medial femoral cartilage, lateral femoral cartilage, and tibial cartilage. Relaxation time values were clipped to a range of 0-100 milliseconds to reduce noise and ensure the results align with clinically meaningful thresholds.

This process was performed for each cartilage region of interest, and an overall total value was calculated by averaging results across all relevant regions for a given slice. Subject-level relaxation times for both T<sub>1ρ</sub> and T<sub>2</sub> mapping were obtained by aggregating the average relaxation times across slices.

By computing these values from both predicted and ground truth segmentations, we captured both the structural properties (from the segmentation masks) and the biochemical properties (from the relaxation

times) of cartilage. This allowed us to evaluate the agreement between model predictions and manual annotations, assessing the model's accuracy in predicting biochemical biomarkers within a clinical context.

### *Intervertebral Disc Height Measurement*

Intervertebral disc height is a clinically valuable biomarker for assessing spinal health, with reductions often indicative of degenerative disc disease. To compute disc height from MRI scans, we utilized segmentation masks to identify the boundaries of each intervertebral disc and measured the vertical distance between their superior and inferior borders.

We identified individual intervertebral disc instances using connected component labeling for manual and model-predicted segmentation masks. Each disc instance was enclosed within a minimal bounding rectangle calculated from the disc's contour, identified using a convex hull. This approach accounts for natural variations in disc shape, including irregular or deformed anatomical structures, enabling accurate measurements for these complex geometries.

Disc height was calculated by measuring the Euclidean distance between the superior and inferior edges of the bounding rectangle derived from the segmentation mask. Measurements were scaled according to the pixel spacing from the MRI metadata, converting pixel units into millimeters. This procedure was applied slice by slice across the MRI scan.

To determine subject-level disc height, we calculated the maximum disc height for each intervertebral disc across all slices. This metric, representing the greatest disc height, enabled direct comparison between predicted and manual measurements, validating the model's ability to replicate clinical assessments accurately. In this way, this method accommodates varying disc shapes and provides precise estimates of geometry and vertical dimensions with use of contour detection and bounding rectangle calculations.

Automated disc height measurements offer clinicians a reliable way to identify degenerative changes or assess post-surgical outcomes. When accurate, they may provide an additional layer of support to manual evaluations in clinical practice.

### *Muscle and Tissue Volume Analysis*

We calculated muscle and tissue volumes for thigh muscles, lumbar spine muscles, knee bones, and hip bones using segmentation masks from both manual annotations and model predictions. Tissue volumes were derived by computing the volume of each segmented region in every MRI slice and summing these volumes across slices to obtain the total tissue volume for each subject, expressed in cubic centimeters (cm<sup>3</sup>).

For each MRI slice, the volume corresponding to the segmented tissue was calculated by summing the number of voxels within the mask and multiplying by the voxel volume. The voxel volume was computed as:

$$\text{Voxel Volume} = \text{pixel spacing}_x \times \text{pixel spacing}_y \times \text{slice thickness}(\text{mm}^3)$$

Thus, the slice volume for each tissue class was calculated:

$$\text{Slice Volume}_{\text{class}} = \text{voxel count}_{\text{class}} \times \text{Voxel Volume} (\text{mm}^3)$$



where  $\text{voxel count}_{\text{class}}$  is the number of voxels in the segmentation mask for the tissue class in that slice. The total volume for each tissue class was obtained by summing the slice volumes across all slices containing the segmented tissue:

$$\text{Total Volume}_{\text{class}} = \sum_{\text{slices}} \text{Slice Volume}_{\text{class}} (\text{mm}^3)$$

To convert the total volume to cubic centimeters, we divided by 1,000:

$$\text{Total Volume}_{\text{class}} (\text{cm}^3) = \frac{\text{Total Volume}_{\text{class}} (\text{mm}^3)}{1,000}$$

This procedure was applied to each anatomical class across all MRI slices, providing detailed volume measurements for each tissue type. Additionally, a total volume combining all tissue classes was computed by aggregating the volumes of all segmented regions.

This method provides accurate estimates of muscle and bone volumes, important biomarkers for assessing musculoskeletal health, and monitoring conditions like sarcopenia, muscle atrophy, and osteoporosis. In this way, these automated volume estimates may support patient counseling, track rehabilitation progress, and facilitate early detection of musculoskeletal conditions. Comprehensive comparisons of all evaluated biomarkers, including muscle and bone volumes, cartilage thickness, relaxation times, and disc height, are provided in Supplementary Tables S39–S64. These results demonstrate the models' ability to replicate clinically relevant measurements across anatomical regions and datasets.

#### *Intraclass Correlation Coefficient (ICC) Analysis*

To quantify the agreement between model-predicted and manual biomarker measurements across subjects, we employed Intraclass Correlation Coefficient (ICC) analyses, selecting methodologies based on the distributional properties of the data (Supplementary Table S65). The Shapiro-Wilk test was used to inspect the normality of biomarker metric distributions, and Levene's test was applied to evaluate their homogeneity of variance. For metrics satisfying both criteria, we utilized the parametric ICC(3,1) model implemented via the *Pingouin*<sup>75</sup> library. This model, based on a two-way mixed-effects ANOVA, focuses on absolute agreement between a fixed set of raters—namely, the manual annotations and model predictions. Confidence intervals were derived using parametric methods based on variance components computed within the *Pingouin* function.

For metrics not meeting normality or homogeneity of variance assumptions, we applied a non-parametric ICC approach using a *Statsmodels*<sup>76</sup> linear mixed-effects model. This model accounts for subject-level variability by including random effects, which captures both between-subject variance and residual variance. The ICC was defined as the ratio of between-subject variance to total variance, accommodating non-normal or unbalanced data distributions.

We performed bootstrap resampling with 10,000 iterations to ensure the reliability of our estimates. In each iteration, subjects were resampled with replacement, maintaining the paired structure between manual and model-predicted metrics. An ICC value was computed for each bootstrap sample, yielding a distribution from which the median ICC was reported for its robustness to skewness and outliers; this aligns with our non-parametric analyses (e.g., Bland-Altman plots in Fig. 5b). The 95% confidence intervals were calculated by identifying the values at the 2.5th and 97.5th percentiles of the bootstrap distribution, which served as the lower and upper bounds, respectively.

This method evaluated the agreement between model-derived and manual biomarker metrics while accounting for their statistical properties (Supplementary Table S66). These exploratory analyses show that model-predicted metrics align well with manual methods and establish a strong base for translating model performance into metrics that could potentially support clinical workflows.

### *Bland-Altman Analysis*

To complement the ICC analysis and provide a visual assessment of agreement across biomarkers, we conducted Bland-Altman analyses, selecting parametric or non-parametric methods based on the distributional properties of the data (Supplementary Table S65). For metrics satisfying normality and homogeneity of variance, we applied the parametric Bland-Altman method using the Pingouin library. This approach computes the mean difference (bias) between the two measurement methods and defines the limits of agreement as the mean difference  $\pm 1.96$  times the standard deviation of the differences, assuming normally distributed differences.

For metrics not meeting these assumptions, we employed a non-parametric Bland-Altman analysis. The median difference between model predictions and manual annotations was calculated, and the limits of agreement were established based on the range from the 2.5th to 97.5th percentiles of the differences; this captures 95% of the data without relying on normal distribution assumptions.

To quantify uncertainty in the non-parametric analyses, we performed bootstrap resampling with 10,000 iterations. Subjects were resampled with replacement for each iteration, and the median and percentile-based agreement limits were recalculated, producing bootstrap distributions. The 95% confidence intervals were then determined as the range between the lower and upper percentiles (2.5th and 97.5th) of these distributions.

In the Bland-Altman plots (Fig. 5b), we plotted the differences between model predictions and manual annotations against their averages. The bias is represented by a horizontal line, with dashed lines indicating the limits of agreement. Shaded regions denote bootstrapped confidence intervals, illustrating the variability in the observed differences.

By combining parametric and non-parametric Bland-Altman analyses, we aimed to diligently evaluate agreement in a manner that is appropriate for the characteristics of each biomarker metric.

### *Regression Analysis for Biomarker Agreement*

To further investigate the relationship between model-predicted and manual biomarker values, we conducted regression analyses appropriate to the data's statistical properties (Supplementary Table S65). For biomarkers satisfying normality and homogeneity of variance, we performed linear regression using the SciPy<sup>74</sup> Stats library to assess the linear relationship between the automated segmentation metrics and manual annotations. Detailed results—including the intercept, slope, Pearson's correlation coefficient (R), coefficient of determination ( $R^2$ ), p-value, and standard error—are provided in Supplementary Table S67. In Fig. 5b, manual annotation values (y-axis) are plotted against automated method values (x-axis), featuring the regression line and the identity line ( $y = x$ ) for direct comparison. The  $R^2$  value and p-value indicate the strength and significance of the linear relationship.

For biomarkers not meeting normality or homogeneity of variance assumptions, we utilized Gaussian Process Regression (GPR) with the scikit-learn library to capture potential non-linear relationships and heteroscedasticity. The GPR model was defined using a composite kernel:

$$K(x, x') = RBF(x, x') + WhiteKernel$$

where the Radial Basis Function (RBF) kernel models smooth variations, and the WhiteKernel accounts for noise in the data. The length scale and noise level hyperparameters were optimized during model fitting. The alpha parameter was set to 0, and *normalize\_y = True* ensured output normalization. The model was fitted with automated biomarker metrics as the independent variable X and manual annotations as the dependent variable y.

Predictions were generated over the range of observed automated metrics, with 95% confidence intervals calculated as:

$$y_{pred} = \pm 1.96 \times y_{std}$$

where *y\_pred* is the predicted mean and *y\_std* is the standard deviation of the predictions. Scatter plots (Fig. 5b) display observed biomarker values along with the GPR regression line and shaded 95% confidence intervals. The identity line ( $y = x$ ) facilitates direct comparison, highlighting deviations from perfect agreement.

We applied parametric linear regression and non-parametric Gaussian Process Regression (GPR) to account for the statistical characteristics of each dataset. This approach ensured a thorough evaluation of the relationship between automated and manual biomarker metrics. The observed agreement in these tests highlights the capability for model-predicted outputs to align with clinically relevant patterns captured in manual annotations, building confidence in their applicability for radiological workflows and patient care.

#### *Spearman's Rank Correlation*

For biomarkers not satisfying normality and homogeneity of variance assumptions, we computed Spearman's rank correlation coefficient ( $\rho$ ) to assess the monotonic relationship between biomarker metrics derived from manual annotations and automated segmentation methods (Supplementary Table S68). Spearman's  $\rho$  ranges from  $-1$  (perfect negative monotonic relationship) to  $+1$  (perfect positive monotonic relationship), with p-values indicating statistical significance.

Biomarker values were compared at the subject level, excluding subjects with missing data. Spearman's  $\rho$  was computed using the *spearmanr* function from the SciPy<sup>74</sup> library.

This analysis provided a non-parametric complement to the Bland-Altman plots and regression analyses. It was particularly useful for exploring relationships between automated and manual biomarker metrics in cases of non-linear or unevenly distributed data. Spearman's rank correlation expanded the scope of evaluation, and enabled a broader assessment of the model's performance across varied data distributions.

#### *Object Detection Model Training for Automated Pipeline*

To evaluate object detection-derived prompts in our automated pipeline, we trained YOLOv8<sup>77</sup> models using five datasets within the Ultralytics framework. We selected YOLOv8 for its robust open-source ecosystem and its alignment with the requirements of system innovation and prototyping, particularly for rapid and reliable bounding box generation. This capability is essential for designing workflows that could, in principle, reduce the manual burden on radiologists or technologists. Its strong community support, ongoing updates, and open-source framework make it a practical choice for advancing medical imaging research. While not positioned as a final deployment-ready tool for clinical use, YOLOv8 provides a

flexible and accessible platform for the development and evaluation of automated pipelines. Its integration facilitated reproducibility and accessibility, supported by abundant resources and tutorials.

YOLOv8 models were trained using the Ultralytics training framework, which allows for straightforward configuration and execution through YAML files. We trained each model using an associated dataset's full training set; in this way, we could establish a fair comparison between the detection and segmentation models. The training process involved defining key parameters such as the model architecture (e.g., YOLOv8, RT-DETR<sup>78</sup>), image size (e.g., 1024×1024 pixels), number of epochs (e.g., 100), batch size (e.g., 8), etc. These configurations were detailed in the corresponding YAML files in a similar manner to our segmentation model pipelines, such that training runs could be tracked reliably.

To further align detection model training with the segmentation workflow, we utilized preprocessed .npy image files and labels derived from the same .npy mask slices, prepared as part of the overall data processing pipeline. It was our intention to produce an efficient data preparation pipeline to benefit both detection and segmentation tasks. Class labels (e.g., femoral cartilage, patellar cartilage) and paths to the training, validation, and test sets were specified in dataset-specific YAML files, which created a structured setup. The training was initiated via a Python script that interfaced with the Ultralytics API, incorporating parameters directly from the YAML files. Resultingly, this method provided consistent training processes through standard data handling and hyperparameter control.

The selection of YOLOv8 was a deliberate and pragmatic choice based on its reliability and accessibility. Our goal was not to advance the development of object detection models, but rather to develop a dependable and easily accessible pipeline for incorporating SAM-based models into current medical imaging workflows. This aligns with broader discussions in the literature, which emphasize the practical adoption of AI models in clinical and research settings. Because of its well-established performance and widespread community support, YOLOv8 is a reliable choice, especially for researchers with different degrees of computational proficiency. Its extensive use guarantees accessibility and reproducibility, two factors that were imperative to the objectives of our study.

This pipeline is not restricted to YOLOv8. Its modular design can easily adapt to the specifications of newer or more sophisticated object detection models as they are developed. We demonstrate a flexible and well-supported tool that accentuates the pipeline's inherent utility. Although some might consider this decision to be unduly simplistic, it offers researchers unfamiliar with these tools a useful starting point. The framework encourages innovation and customization, enabling them to adapt the pipeline as new detection models emerge from academic and industry efforts.

### *Configuration and Setup for Prediction-Based Segmentation*

The pipeline managed model parameters, pipeline settings, and dataset details using a YAML configuration system. Similar to the evaluation pipelines for standard segmentation metrics and biomarkers, this systematic design allowed clean experiment tracking and replication. Although speculative for clinical IT applications, this design aligns with the need for systems that manage model adaptation and updating efficiently; such configurations could support reproducible evaluations and informed decisions when new patient data, model updates, or population changes require internal testing and verification. By enabling efficient modifications to experimental setups without altering the underlying code, this approach demonstrates the potential for fostering adaptability in clinical imaging workflows.

### *Modular Data Handling and Preprocessing*

The pipeline employed a modular data module to handle dataset metadata and construct loaders for segmentation evaluation. Standardization of preprocessing steps across datasets allowed detection and

segmentation tasks to align, which provided consistent inputs for the models. This uniformity supports reproducibility and facilitates cross-study comparisons, providing a robust foundation for research applications and potential clinical adaptability.

### *Integration of Object Detection and Segmentation Models*

Object detection and segmentation models were integrated via a centralized Tester class. During the evaluation run, YOLOv8 could generate bounding boxes from MRI slices; these bounding boxes, representing anatomical structures, served as the prompts for the segmentation models. Models were pre-configured with baseline or finetuned weights, and bounding boxes were resized as needed to ensure compatibility with segmentation inputs. This integration demonstrates an efficient method for linking detection and segmentation tasks, which reduces manual effort and ensures consistency and efficiency in imaging workflows.

### *Evaluation Loop and Mask Generation Workflow*

During evaluation, batches of MRI slices were processed iteratively. YOLOv8 identified regions of interest, providing bounding boxes with class IDs as prompts for segmentation models. Predicted masks were generated from segmentation logits, which were converted into binary masks using a sigmoid function and a threshold of 0.5. This approach supports consistent segmentation generation across diverse patients or imaging sequences and lessens the dependency on manual oversight.

### *Post-Processing and Mask Refinement Techniques*

Post-processing steps, implemented using OpenCV<sup>79</sup>, were applied to segmentation outputs to improve quality and anatomical accuracy. Small, isolated regions were removed through connected component analysis, and morphological operations such as closing (dilation followed by erosion) were used to fill gaps and create cohesive segmentations. Kernel sizes for these operations were tailored to each anatomical region to preserve structural details while addressing gaps. Gaussian blurring was also applied to smooth mask edges and reduce abrupt transitions, and a binary threshold was reapplied to finalize the masks for evaluation. These refinements align masks with anatomical expectations, supporting workflows where segmentation quality impacts clinical confidence.

### *Evaluation Metrics and Performance Analysis*

Dice similarity coefficients and Intersection over Union (IoU) scores were used to evaluate segmentation performance. Results were generated at the subject and dataset levels by aggregating metrics computed for individual MRI slices; structured summaries of slice-level metrics were exported in CSV and JSON formats. These outputs facilitated detailed comparisons and cross-model analyses, providing insights into model performance under automated prompt conditions. The framework is centered on Dice and IoU metrics in this analysis but could be adapted to include biomarker-based evaluations for greater flexibility in future prompt-based model analyses.

### *Visualization and Qualitative Assessment of Results*

To complement quantitative metrics, the pipeline generated visual overlays of YOLOv8-predicted bounding boxes and segmentation masks on MRI slices. Visualizations were generated at regular intervals, such as every tenth slice, to demonstrate detection and segmentation interactions. The images were stored in dedicated directories for easy review and qualitative analysis.

### *Overview of the Automatic Pipeline for Object Detection and Segmentation*

The AutoLabel Pipeline was developed to address the practical limitations of integrating SAM and SAM2-based segmentation models into large-scale medical imaging workflows. These models rely on prompts, such as bounding boxes or points, to produce accurate segmentations. In musculoskeletal (MSK) research, where 3D MRI datasets often contain hundreds of slices, manually generating these prompts is both impractical and time-intensive, creating a significant barrier to scalability.

This analysis focuses on evaluating the performance of SAM and SAM2-based models when using bounding box prompts generated by YOLOv8. As these prompts are not derived from ground truth masks, they provide a pragmatic test of how the models handle inaccuracies. Our goal in conducting this assessment was to ascertain whether segmentation masks could be consistently and automatically produced without the need for human involvement.

The objective is to create an automated, scalable process that strikes a balance between efficiency and segmentation accuracy. This would enable researchers to concentrate on downstream tasks, such as tissue analysis and dataset construction, without the bottleneck of manual prompt creation.

### *Experimental Setup for Model and Dataset Evaluation*

For this analysis, we evaluated five segmentation models across five datasets: Thigh\_2D\_T1ax\_Clinical\_Anatomical\_50, Shoulder\_3D\_CUBE\_Research\_Anatomical\_28, Spine\_2D\_T1sag\_Clinical\_Anatomical\_23, Knee\_3D\_DESS\_Research\_Anatomical\_86, and Spine\_2D\_T1ax\_Clinical\_Anatomical\_59. These datasets represent anatomies commonly seen in musculoskeletal radiology and demonstrate the potential clinical value of improved performance for patient evaluations and interventional planning. Three models, SAM, MedSAM, and SAM2, were assessed in their zero-shot form (without finetuning). Additionally, we included the best-performing finetuned model for each dataset, with and without bounding box augmentation shift, to examine how model performance varied across different prompt conditions.

### *Prediction Refinement and Evaluation Workflow*

After obtaining the predicted segmentation masks from the models, we applied a post-processing pipeline to refine the outputs before evaluation. The logits were converted into binary masks using a sigmoid function followed by thresholding at 0.5, resulting in binary predictions indicating background (0) or object (1). Small, isolated objects were removed using connected component analysis to eliminate noise, ensuring that only meaningful segmentation regions remained.

Morphological closing was then applied to the cleaned masks, involving dilation followed by erosion, to close small gaps and holes within the predicted regions for more cohesive and anatomically plausible segmentations. The kernel size for morphological operations was chosen based on the dataset and class labels, with values ranging from smaller kernels ( $7 \times 7$ ) for finer-detail labels to larger kernels ( $15 \times 15$ ) for coarser labels, balancing gap filling with preservation of structural integrity. A Gaussian blur, matching the kernel size of the morphological operations, was applied to smooth the boundaries of the segmented regions, reducing sharp transitions between foreground and background pixels.

Segmentation performance was evaluated by computing Dice similarity scores on a slice-by-slice basis for each MRI volume. These individual slice scores were aggregated to determine the mean Dice score at the subject level, as well as the dataset level (Supplementary Tables S69–S70). This post-processing pipeline not only eliminated noise and refined mask structures but also ensured accurate Dice score evaluations for subsequent analysis.

For statistical comparisons of model performance, we applied pairwise Wilcoxon rank-sum tests, adjusting for multiple comparisons using the Benjamini-Hochberg correction (Supplementary Table S71). Results

are visualized using raincloud plots, which combine box plots and density plots to display the full distribution of Dice scores for each model and dataset. The raincloud plots for all five datasets and five models are shown in Fig. 5c, accentuating performance differences across models when using different prompt types, including ground truth-derived and YOLOv8-generated prompts.

Supplementary Figures 11–15 provide detailed visual comparisons for the segmentation models on each dataset, including SAM, SAM2, MedSAM, and finetuned models (with and without bounding box shift augmentation). Each figure presents five plots across three representative subjects: (1) the original MRI slice with YOLOv8-predicted bounding boxes, (2) the ground truth segmentation overlay, (3) the predicted segmentation overlay, (4) the ground truth contour, and (5) the predicted contour. The visualizations display how YOLOv8-generated bounding box prompts impact segmentation accuracy. They provide insight into the models' ability to produce reliable masks when faced with realistic, imperfect prompts.

### *Automated Segmentation for Large-Scale Medical Imaging*

The AutoLabel system is made to segment unlabeled medical imaging datasets completely automatically, allowing for scalable and effective workflows. By integrating object detection and segmentation models, the system processes raw medical imaging data, such as DICOM or NIfTI volumes, into segmentation masks ready for downstream analysis. This workflow is particularly valuable for musculoskeletal (MSK) MRI datasets, where the scale and complexity of 3D imaging volumes presents substantial challenges for manual segmentation. Automation in high-volume clinical MRI environments has the potential to accelerate patient workflows and decrease radiologist fatigue while having the potential to enhance efficiency and diagnostic reliability through standardized processes. AutoLabel ensures consistency and lessens the workload associated with human intervention by doing away with the need for user-provided prompts.

### *System Workflow and Modular Architecture*

The system processes imaging data as three-dimensional volumes by performing slice-by-slice object detection and segmentation. Detection models generate bounding box prompts, which are fed into segmentation models to produce binary masks. These outputs are then assembled into comprehensive 3D masks. Because the pipeline is modular, users can incorporate different detection or segmentation models to customize the workflow to suit different study requirements.

Input data is ingested from either individual files or directories of DICOM slices or NIfTI volumes. For DICOM datasets, slices are sorted by instance number to ensure accurate spatial alignment before preprocessing. Key preprocessing steps include intensity normalization, resizing to meet model requirements, and formatting single-channel images into three-channel tensors. These standardized inputs are transferred to the GPU for efficient inference, streamlining data preparation without manual adjustments.

### *Integrated Inference and Mask Refinement*

The AutoLabel system automates the detection-to-segmentation workflow, leveraging YOLOv8 detection models and SAM-based segmentation models developed earlier in the methods. Object detection outputs bounding boxes for each slice, which serve as prompts for segmentation models to produce binary masks. These slice-wise results are then aggregated into volumetric segmentation outputs.

Post-processing techniques, consistent with the refinement methods outlined earlier, are applied to enhance segmentation masks. These steps include Gaussian blurring, morphological operations, and thresholding to ensure anatomical plausibility and minimize noise. Masks are resized to original image dimensions for accurate spatial correspondence, and isolated regions are removed to enhance segmentation quality. This ensures that output is robust and ready for downstream use.

### *Visualization Tools and Data Output Management*

The system includes optional visualization features that overlay segmentation masks on original image slices for qualitative review. These visualizations generated periodically (e.g., every fifth slice), enable researchers to assess segmentation accuracy and monitor data quality. In accordance with standard procedures, outputs are stored as 3D NIfTI volumes in organized directories, which makes compatibility with widely used medical imaging tools easier.

### *Applications and Scalability in Clinical Research*

AutoLabel provides a reproducible framework for fully automatic segmentation, addressing the needs of researchers working with large-scale medical imaging datasets. In addition to supporting effective workflows through the integration of preprocessing, inference, and post-processing, its modular design promotes adaptability to new models and technologies. AutoLabel's segmentation automation simplifies tasks like biomarker extraction and dataset construction and supports broader adoption in clinical research. This system's scalability could benefit population-level studies and routine imaging tasks; its consistent and efficient solutions have applications in orthopedics, sports medicine, and precision imaging.

### **Data availability**

The Osteoarthritis Initiative (OAI) dataset used in this study is publicly available at <https://nda.nih.gov/oai>. Other MRI datasets, including segmentation masks, were collected under Institutional Review Board (IRB) approval and can be requested from the authors in compliance with UCSF data-sharing agreements. Processed data, including statistical analyses and metrics derived from the segmentation models, are provided in the supplementary materials to support reproducibility and further research.

### **Code availability**

<https://github.com/gabbieHoyer/AutoMedLabel>

### **Acknowledgements**

We thank D. Lansdown, T.M. Link, B. Ma, and R.B. Souza for their leadership in advancing research on musculoskeletal health, particularly in understanding disease mechanisms, patient risk factors, and responses to treatment. We acknowledge E. Bahroos and M. Han for their work in optimizing fat-suppressed CUBE sequence acquisition parameters. We are grateful to Z. Akkaya, U. Bharadwaj, C. Chin, F.G. Gassert, P.J. Giesler, G. Inamda, V. Kreutzinger, J. Lutigens, V. Wang, and K. Ziegeler for their contributions to dataset labeling across segmentation tasks. Finally, we thank A. Beltran, J. Cummings, K.T. Gao, M. Hess, N. Konovalova, J. Lee, F. Liu, E. Ozhinsky, F. Su, R. Thahakoya, and A. Tolpadi for their efforts in data refinement, cleaning, and aggregation for further analysis. We also thank A. Becker, J. Chan, P. Storey, L. Torres, and B. Yazel for their support in managing data infrastructure, technical operations, and high-performance computing resources. We extend our gratitude to the many members of the Musculoskeletal Quantitative Imaging Research (MQIR) group for their contributions and support in advancing musculoskeletal imaging research. This research was funded by the National Institute of Arthritis and Musculoskeletal and Skin Diseases (NIH-NIAMS) through several grants, including: NIH R01AR069006, "Evaluating Disease Progression in Hip Osteoarthritis"; NIH UH3AR076724/4UH3AR076724-02, "Technology Research Site for Advanced, Faster Quantitative Imaging for BACPAC"; NIH R00AR070902, "Multidimensional MRI-based Non-Euclidean Deep Learning to Study Osteoarthritis"; NIH R01AR078762, "Ultra-Fast Knee MRI with Deep Learning"; NIH P50AR060752 and R61AR073552/ R33AR073552, supporting the Osteoarthritis Initiative (OAI); and NIH R01AR0796471. Additional support includes NIH R01AR046905 for studies on grading abnormalities in musculoskeletal imaging, and NIH R01AR078917 as part of the OAI's efforts in examining osteoarthritis progression. The OAI, a public-private partnership supported by NIH contracts (N01-AR-2-2258; N01-AR-2-2259; N01-AR-2-2260; N01-AR-2-2261; N01-AR-2-2262), also received funding through the Foundation for the NIH, with contributions from Merck, Novartis, GlaxoSmithKline, and Pfizer.



## Authors' contributions

All authors contributed to the conception and design of the study, as well as to the preparation and approval of the manuscript and supplementary materials. G.H. developed the software infrastructure, including metadata management, model finetuning, evaluation pipelines, and the automated AutoLabel inference system. Data aggregation and preprocessing were carried out by G.H. and M.W.T., providing a unified basis for analysis. Model training, finetuning, and evaluation were conducted by G.H. Statistical design was a collaborative effort among G.H., V.P., and S.M., with G.H. conducting the analysis and V.P. and S.M. performing technical verification. Biomarker evaluation was jointly ideated by all authors, with implementation and analysis executed by G.H.; contributions from M.W.T. and R.B. in data preparation and results validation were integral to the process. V.P. and S.M. provided leadership in conceptualizing the study, securing funding, and offering valuable input during the manuscript revision process.

## Competing interests

The authors declare no competing interests.

## References

1. Litjens, G. *et al.* A survey on deep learning in medical image analysis. *Medical Image Analysis* **42**, 60–88 (2017).
2. Zhou, S. K. *et al.* A Review of Deep Learning in Medical Imaging: Imaging Traits, Technology Trends, Case Studies With Progress Highlights, and Future Promises. *Proc. IEEE* **109**, 820–838 (2021).
3. Ronneberger, O., Fischer, P. & Brox, T. U-Net: Convolutional Networks for Biomedical Image Segmentation. in *Medical Image Computing and Computer-Assisted Intervention – MICCAI 2015* (eds. Navab, N., Hornegger, J., Wells, W. M. & Frangi, A. F.) vol. 9351 234–241 (Springer International Publishing, Cham, 2015).
4. Milletari, F., Navab, N. & Ahmadi, S.-A. V-Net: Fully Convolutional Neural Networks for Volumetric Medical Image Segmentation. Preprint at <https://doi.org/10.48550/ARXIV.1606.04797> (2016).
5. Zhou, Z., Rahman Siddiquee, M. M., Tajbakhsh, N. & Liang, J. UNet++: A Nested U-Net Architecture for Medical Image Segmentation. in *Deep Learning in Medical Image Analysis and Multimodal Learning for Clinical Decision Support* (eds. Stoyanov, D. *et al.*) vol. 11045 3–11 (Springer International Publishing, Cham, 2018).
6. Jha, D. *et al.* ResUNet++: An Advanced Architecture for Medical Image Segmentation. Preprint at <https://doi.org/10.48550/ARXIV.1911.07067> (2019).
7. Oktay, O. *et al.* Attention U-Net: Learning Where to Look for the Pancreas. Preprint at <https://doi.org/10.48550/ARXIV.1804.03999> (2018).
8. Isensee, F., Jaeger, P. F., Kohl, S. A. A., Petersen, J. & Maier-Hein, K. H. nnU-Net: a self-configuring method for deep learning-based biomedical image segmentation. *Nat Methods* **18**, 203–211 (2021).

9. Cao, H. *et al.* Swin-Unet: Unet-like Pure Transformer for Medical Image Segmentation. Preprint at <https://doi.org/10.48550/ARXIV.2105.05537> (2021).
10. Guan, H. & Liu, M. Domain Adaptation for Medical Image Analysis: A Survey. *IEEE Trans. Biomed. Eng.* **69**, 1173–1185 (2022).
11. Tajbakhsh, N. *et al.* Embracing imperfect datasets: A review of deep learning solutions for medical image segmentation. *Medical Image Analysis* **63**, 101693 (2020).
12. Yan, W. *et al.* MRI Manufacturer Shift and Adaptation: Increasing the Generalizability of Deep Learning Segmentation for MR Images Acquired with Different Scanners. *Radiology: Artificial Intelligence* **2**, e190195 (2020).
13. Kirillov, A. *et al.* Segment Anything. *arXiv:2304.02643* (2023).
14. Ravi, N. *et al.* SAM 2: Segment Anything in Images and Videos. *arXiv preprint arXiv:2408.00714* (2024).
15. Mazurowski, M. A. *et al.* Segment anything model for medical image analysis: An experimental study. *Medical Image Analysis* **89**, 102918 (2023).
16. He, S. *et al.* Computer-Vision Benchmark Segment-Anything Model (SAM) in Medical Images: Accuracy in 12 Datasets. Preprint at <https://doi.org/10.48550/ARXIV.2304.09324> (2023).
17. Huang, Y. *et al.* Segment Anything Model for Medical Images? (2023) [doi:10.48550/ARXIV.2304.14660](https://doi.org/10.48550/ARXIV.2304.14660).
18. Ma, J. *et al.* Segment anything in medical images. *Nat Commun* **15**, 654 (2024).
19. Chen, C. *et al.* MA-SAM: Modality-agnostic SAM Adaptation for 3D Medical Image Segmentation. Preprint at <https://doi.org/10.48550/ARXIV.2309.08842> (2023).
20. Zhang, K. & Liu, D. Customized Segment Anything Model for Medical Image Segmentation. Preprint at <https://doi.org/10.48550/ARXIV.2304.13785> (2023).
21. Dong, H. *et al.* Segment anything model 2: an application to 2D and 3D medical images. Preprint at <https://doi.org/10.48550/ARXIV.2408.00756> (2024).
22. Ma, J. *et al.* Segment Anything in Medical Images and Videos: Benchmark and Deployment. Preprint at <https://doi.org/10.48550/ARXIV.2408.03322> (2024).
23. Plewes, D. B. & Kucharczyk, W. Physics of MRI: A primer. *Magnetic Resonance Imaging* **35**, 1038–1054 (2012).
24. Florkow, M. C. *et al.* Magnetic Resonance Imaging Versus Computed Tomography for Three-Dimensional Bone Imaging of Musculoskeletal Pathologies: A Review. *Magnetic Resonance Imaging* **56**, 11–34 (2022).
25. Hussain, S. *et al.* Modern Diagnostic Imaging Technique Applications and Risk Factors in the Medical Field: A Review. *BioMed Research International* **2022**, 1–19 (2022).

26. Peterfy, C. G. *et al.* Whole-Organ Magnetic Resonance Imaging Score (WORMS) of the knee in osteoarthritis. *Osteoarthritis and Cartilage* **12**, 177–190 (2004).
27. Wen, P. Y. *et al.* Response Assessment in Neuro-Oncology Clinical Trials. *JCO* **35**, 2439–2449 (2017).
28. Turkbey, B. *et al.* Prostate Imaging Reporting and Data System Version 2.1: 2019 Update of Prostate Imaging Reporting and Data System Version 2. *European Urology* **76**, 340–351 (2019).
29. Salmond, S. & Dorsen, C. Time to Reflect and Take Action on Health Disparities and Health Inequities. *Orthopaedic Nursing* **41**, 64–85 (2022).
30. Chen, N., Fong, D. Y. T. & Wong, J. Y. H. Health and Economic Outcomes Associated With Musculoskeletal Disorders Attributable to High Body Mass Index in 192 Countries and Territories in 2019. *JAMA Netw Open* **6**, e2250674 (2023).
31. Briggs, A. M. *et al.* Context and priorities for health systems strengthening for pain and disability in low- and middle-income countries: a secondary qualitative study and content analysis of health policies. *Health Policy and Planning* **38**, 129–149 (2023).
32. Nguyen, A. T. *et al.* Musculoskeletal health: an ecological study assessing disease burden and research funding. *The Lancet Regional Health - Americas* **29**, 100661 (2024).
33. Müller, D., Soto-Rey, I. & Kramer, F. Towards a guideline for evaluation metrics in medical image segmentation. *BMC Res Notes* **15**, 210 (2022).
34. Hirling, D. *et al.* Segmentation metric misinterpretations in bioimage analysis. *Nat Methods* (2023) doi:10.1038/s41592-023-01942-8.
35. Loeser, R. F., Goldring, S. R., Scanzello, C. R. & Goldring, M. B. Osteoarthritis: A disease of the joint as an organ. *Arthritis & Rheumatism* **64**, 1697–1707 (2012).
36. Haig, A. J. Paraspinal denervation and the spinal degenerative cascade. *The Spine Journal* **2**, 372–380 (2002).
37. Cruz-Jentoft, A. J. *et al.* Sarcopenia: revised European consensus on definition and diagnosis. *Age and ageing* **48**, 16–31 (2019).
38. Iriondo, C. *et al.* Towards understanding mechanistic subgroups of osteoarthritis: 8-year cartilage thickness trajectory analysis. *Journal of Orthopaedic Research®* **39**, 1305–1317 (2021).
39. Cummings, J. *et al.* The knee connectome: A novel tool for studying spatiotemporal change in cartilage thickness. *Journal Orthopaedic Research* **42**, 43–53 (2024).
40. Morales, A. G. *et al.* Uncovering associations between data-driven learned qMRI biomarkers and chronic pain. *Scientific reports* **11**, 21989 (2021).

41. Pedoia, V., Lee, J., Norman, B., Link, T. M. & Majumdar, S. Diagnosing osteoarthritis from T2 maps using deep learning: an analysis of the entire Osteoarthritis Initiative baseline cohort. *Osteoarthritis and cartilage* **27**, 1002–1010 (2019).
42. Han, M., Tibrewala, R., Bahroos, E., Pedoia, V. & Majumdar, S. Magnetization-prepared spoiled gradient-echo snapshot imaging for efficient measurement of  $R_2 - R_{1\rho}$  in knee cartilage. *Magnetic Resonance in Med* **87**, 733–745 (2022).
43. Carballido-Gamio, J., Joseph, G. B., Lynch, J. A., Link, T. M. & Majumdar, S. Longitudinal analysis of MRI  $T_2$  knee cartilage laminar organization in a subset of patients from the osteoarthritis initiative: A texture approach. *Magnetic Resonance in Med* **65**, 1184–1194 (2011).
44. Iriundo, C., Pedoia, V. & Majumdar, S. Lumbar intervertebral disc characterization through quantitative MRI analysis: An automatic voxel-based relaxometry approach. *Magnetic Resonance in Med* **84**, 1376–1390 (2020).
45. Hess, M. *et al.* Deep Learning for Multi-Tissue Segmentation and Fully Automatic Personalized Biomechanical Models from BACPAC Clinical Lumbar Spine MRI. *Pain Medicine* **24**, S139–S148 (2023).
46. Baum, T. *et al.* Association of Quadriceps Muscle Fat With Isometric Strength Measurements in Healthy Males Using Chemical Shift Encoding-Based Water-Fat Magnetic Resonance Imaging: *Journal of Computer Assisted Tomography* **40**, 447–451 (2016).
47. Bhattacharjee, R. *et al.* Exploring Bilateral Thigh Normalized-Lean-Muscle And Fat Volume Associations With Knee Cartilage Thickness And Functional Parameters In Radiographic Hip Oa Patients. *Osteoarthritis and Cartilage* **31**, S110–S111 (2023).
48. Davison, M. J. *et al.* Lean muscle volume of the thigh has a stronger relationship with muscle power than muscle strength in women with knee osteoarthritis. *Clinical Biomechanics* **41**, 92–97 (2017).
49. Nardo, L. *et al.* Quantitative assessment of fat infiltration in the rotator cuff muscles using water-fat MRI: Fat Infiltration in the Rotator Cuff Muscles. *J. Magn. Reson. Imaging* **39**, 1178–1185 (2014).
50. Roach, K. E., Bird, A. L., Pedoia, V., Majumdar, S. & Souza, R. B. Automated evaluation of hip abductor muscle quality and size in hip osteoarthritis: Localized muscle regions are strongly associated with overall muscle quality. *Magnetic Resonance Imaging* **111**, 237–245 (2024).
51. Hodges, P. W. & Danneels, L. Changes in Structure and Function of the Back Muscles in Low Back Pain: Different Time Points, Observations, and Mechanisms. *Journal of Orthopaedic & Sports Physical Therapy* **49**, 464–476 (2019).
52. Goubert, D., Oosterwijck, J. V., Meeus, M. & Danneels, L. Structural Changes of Lumbar Muscles in Non-specific Low Back Pain: A Systematic Review. *Pain Physician* **19**, E985–E1000 (2016).

53. Liu, F. SUSAN: segment unannotated image structure using adversarial network. *Magnetic Resonance in Med* **81**, 3330–3345 (2019).
54. Vaidyanathan, A. *et al.* Deep learning for the fully automated segmentation of the inner ear on MRI. *Sci Rep* **11**, 2885 (2021).
55. Jia, Z. *et al.* The importance of resource awareness in artificial intelligence for healthcare. *Nat Mach Intell* **5**, 687–698 (2023).
56. Gandhi, T. K. *et al.* How can artificial intelligence decrease cognitive and work burden for front line practitioners? *JAMIA Open* **6**, ooad079 (2023).
57. Tolpadi, A. A. *et al.* K2S Challenge: From Undersampled K-Space to Automatic Segmentation. *Bioengineering* **10**, 267 (2023).
58. Pedoia, V. *et al.* Principal component analysis-T1 $\rho$  voxel based relaxometry of the articular cartilage: a comparison of biochemical patterns in osteoarthritis and anterior cruciate ligament subjects. *Quant. Imaging Med. Surg.* **6**, 623–633 (2016).
59. Osteoarthritis Initiative (OAI), a multi-center, longitudinal, prospective observational study of knee osteoarthritis, sponsored by the National Institutes of Health (NIH) and private industry partners.
60. *White Paper: Imorphics OA Knee MRI Measurements.* www.imorphics.com (2017).
61. Thahakoya, Rafeek. Evaluating the relationship of proximal bone shape asymmetry with cartilage health and biomechanics in patients with hip OA. in (Toronto, Canada, 2023).
62. Gallo, M. C. *et al.* T1 $\rho$  and T2 relaxation times are associated with progression of hip osteoarthritis. *Osteoarthritis and Cartilage* **24**, 1399–1407 (2016).
63. Lee, S. *et al.* Magnetic resonance rotator cuff fat fraction and its relationship with tendon tear severity and subject characteristics. *Journal of Shoulder and Elbow Surgery* **24**, 1442–1451 (2015).
64. Brett, M. *et al.* nipy/nibabel: 3.2.1. Zenodo <https://doi.org/10.5281/ZENODO.4295521> (2020).
65. Lowekamp, B. C., Chen, D. T., Ibáñez, L. & Blezek, D. The Design of SimpleITK. *Front. Neuroinform.* **7**, (2013).
66. Mason, D. *et al.* pydicom/pydicom: Pydicom v2.4.0. Zenodo <https://doi.org/10.5281/ZENODO.8034250> (2023).
67. Biewald, L. Experiment Tracking with Weights and Biases. (2020).
68. Cardoso, M. J. *et al.* MONAI: An open-source framework for deep learning in healthcare. Preprint at <https://doi.org/10.48550/ARXIV.2211.02701> (2022).
69. Paszke, A. *et al.* PyTorch: An Imperative Style, High-Performance Deep Learning Library. Preprint at <https://doi.org/10.48550/ARXIV.1912.01703> (2019).
70. Loshchilov, I. & Hutter, F. Decoupled Weight Decay Regularization. Preprint at <https://doi.org/10.48550/ARXIV.1711.05101> (2017).

71. Loshchilov, I. & Hutter, F. SGDR: Stochastic Gradient Descent with Warm Restarts. Preprint at <https://doi.org/10.48550/ARXIV.1608.03983> (2016).
72. Nickolls, J., Buck, I., Garland, M. & Skadron, K. Scalable Parallel Programming with CUDA: Is CUDA the parallel programming model that application developers have been waiting for? *Queue* **6**, 40–53 (2008).
73. Pedregosa, F. *et al.* Scikit-learn: Machine learning in Python. *the Journal of machine Learning research* **12**, 2825–2830 (2011).
74. Virtanen, P. *et al.* SciPy 1.0: fundamental algorithms for scientific computing in Python. *Nat Methods* **17**, 261–272 (2020).
75. Vallat, R. Pingouin: statistics in Python. *Journal of Open Source Software* **3**, 1026 (2018).
76. Josef Perktold *et al.* statsmodels/statsmodels: Release 0.14.2. Zenodo <https://doi.org/10.5281/ZENODO.10984387> (2024).
77. Jocher, G., Qiu, J. & Chaurasia, A. Ultralytics YOLO. (2023).
78. Zhao, Y. *et al.* Detrs beat yolos on real-time object detection. in *Proceedings of the IEEE/CVF Conference on Computer Vision and Pattern Recognition* 16965–16974 (2024).
79. Bradski, G. The OpenCV Library. *Dr. Dobb's Journal of Software Tools* (2000).